



## An improved total and tropospheric NO<sub>2</sub> column retrieval for GOME-2

Song Liu<sup>1</sup>, Pieter Valks<sup>1</sup>, Gaia Pinardi<sup>2</sup>, Isabelle De Smedt<sup>2</sup>, Huan Yu<sup>2</sup>, Steffen Beirle<sup>3</sup>, and Andreas Richter<sup>4</sup>

<sup>1</sup>Deutsches Zentrum für Luft- und Raumfahrt (DLR), Institut für Methodik der Fernerkundung (IMF), Oberpfaffenhofen, Germany

<sup>2</sup>Belgian Institute for Space Aeronomy (BIRA-IASB), Brussels, Belgium

<sup>3</sup>Max Planck Institute for Chemistry, Mainz, Germany

<sup>4</sup>Institute of Environmental Physics (IUP-UB), University of Bremen, Bremen, Germany

**Correspondence:** Song Liu (Song.Liu@dlr.de)

Received: 16 July 2018 – Discussion started: 6 August 2018

Revised: 14 January 2019 – Accepted: 17 January 2019 – Published: 18 February 2019

**Abstract.** An improved algorithm for the retrieval of total and tropospheric nitrogen dioxide (NO<sub>2</sub>) columns from the Global Ozone Monitoring Experiment-2 (GOME-2) is presented. The refined retrieval will be implemented in a future version of the GOME Data Processor (GDP) as used by the EUMETSAT Satellite Application Facility on Atmospheric Composition and UV Radiation (AC-SAF). The first main improvement is the application of an extended 425–497 nm wavelength fitting window in the differential optical absorption spectroscopy (DOAS) retrieval of the NO<sub>2</sub> slant column density, based on which initial total NO<sub>2</sub> columns are computed using stratospheric air mass factors (AMFs). Updated absorption cross sections and a linear offset correction are used for the large fitting window. An improved slit function treatment is applied to compensate for both long-term and in-orbit drift of the GOME-2 slit function. Compared to the current operational (GDP 4.8) dataset, the use of these new features increases the NO<sub>2</sub> columns by  $\sim 1\text{--}3 \times 10^{14}$  molec cm<sup>2</sup> and reduces the slant column error by  $\sim 24\%$ . In addition, the bias between GOME-2A and GOME-2B measurements is largely reduced by adopting a new level 1b data version in the DOAS retrieval. The retrieved NO<sub>2</sub> slant columns show good consistency with the Quality Assurance for Essential Climate Variables (QA4ECV) retrieval with a good overall quality. Second, the STRatospheric Estimation Algorithm from Mainz (STREAM), which was originally developed for the TROPOspheric Monitoring Instrument (TROPOMI) in-

strument, was optimised for GOME-2 measurements to determine the stratospheric NO<sub>2</sub> column density. Applied to synthetic GOME-2 data, the estimated stratospheric NO<sub>2</sub> columns from STREAM shows good agreement with the a priori truth. An improved latitudinal correction is introduced in STREAM to reduce the biases over the subtropics. Applied to GOME-2 measurements, STREAM largely reduces the overestimation of stratospheric NO<sub>2</sub> columns over polluted regions in the GDP 4.8 dataset. Third, the calculation of AMF applies an updated box-air-mass factor (box-AMF) look-up table (LUT) calculated using the latest version 2.7 of the Vector-Linearized Discrete Ordinate Radiative Transfer (VLIDORT) model with an increased number of reference points and vertical layers, a new GOME-2 surface albedo climatology, and improved a priori NO<sub>2</sub> profiles obtained from the TM5-MP chemistry transport model. A large effect (mainly enhancement in summer and reduction in winter) on the retrieved tropospheric NO<sub>2</sub> columns by more than 10% is found over polluted regions. To evaluate the GOME-2 tropospheric NO<sub>2</sub> columns, an end-to-end validation is performed using ground-based multiple-axis DOAS (MAXDOAS) measurements. The validation is illustrated for six stations covering urban, suburban, and background situations. Compared to the GDP 4.8 product, the new dataset presents improved agreement with the MAXDOAS measurements for all the stations.

## 1 Introduction

Nitrogen dioxide (NO<sub>2</sub>) is an important trace gas in the Earth's atmosphere. In the stratosphere, NO<sub>2</sub> is strongly related to halogen compound reactions and ozone destruction (Solomon, 1999). In the troposphere, nitrogen oxides (NO<sub>x</sub> = NO<sub>2</sub> + NO) serve as a precursor of ozone in the presence of volatile organic compounds (VOCs) and of secondary aerosol through gas-to-particle conversion (Seinfeld et al., 1998). As a prominent air pollutant affecting human health and ecosystems, large amounts of NO<sub>2</sub> are produced in the boundary layer by industrial processes, power generation, transportation, and biomass burning over polluted hot spots. For instance, a strong growth of NO<sub>2</sub> during the past 2 decades has caused severe air pollution problems for China, with the largest NO<sub>2</sub> columns in 2011; since then, cleaner techniques and stricter controlling have been applied to reduce the NO<sub>2</sub> pollution (Richter et al., 2005; van der A et al., 2017; Liu et al., 2017). An increase in NO<sub>2</sub> concentrations due to economic growth is also found over India, with a peak in 2012 (Hilboll et al., 2017). Despite the decrease in NO<sub>x</sub> emissions in Europe, around half of European Union member states still exceed the air quality standards, mainly caused by diesel car emissions (European Commission, 2017).

NO<sub>2</sub> column measurements have been provided by satellite instruments, e.g. Global Ozone Monitoring Experiment (GOME) (Burrows et al., 1999), SCanning Imaging Absorption SpectroMeter for Atmospheric CHartography (SCIAMACHY) (Bovensmann et al., 1999), Ozone Monitoring Instrument (OMI) (Levelt et al., 2006), and Global Ozone Monitoring Experiment-2 (GOME-2) (Callies et al., 2000; Munro et al., 2016). NO<sub>2</sub> observations will be continued by the new generation instruments with high spatial resolution such as TROPOspheric Monitoring Instrument (TROPOMI) (launched in October 2017; Veefkind et al., 2012) and by geostationary missions such as Sentinel-4 (Ingmann et al., 2012). The GOME-2 instrument, which is the main focus of this study, is included on a series of MetOp satellites as part of the EUMETSAT Polar System (EPS). The first GOME-2 was launched in October 2006 aboard the MetOp-A satellite, and a second GOME-2 was launched in September 2012 aboard MetOp-B. The consistent long-term dataset will be further extended by the third GOME-2 on the upcoming MetOp-C platform (to be launched in September 2018). NO<sub>2</sub> measurements from GOME-2 have been widely used to characterise the distribution, evolution, or transport of NO<sub>2</sub> (e.g. Hilboll et al., 2013, 2017; Zien et al., 2014), to estimate the NO<sub>x</sub> emission (e.g. Gu et al., 2014; Miyazaki et al., 2017; Ding et al., 2017), and to interpret VOC levels, ozone variation, or anthropogenic aerosol loading (e.g. Vrekoussis et al., 2010; Safieddine et al., 2013; Penning de Vries et al., 2015).

The GOME-2 total and tropospheric NO<sub>2</sub> products are generated using the GOME Data Processor (GDP) algorithm at the German Aerospace Center (DLR). The retrieval algorithm has been first described by Valks et al. (2011) as imple-

mented in the GDP version 4.4 and was later updated to the current operational version 4.8 (Valks et al., 2017). The NO<sub>2</sub> retrieval for GOME-2 follows a classical three-step scheme.

First, the total NO<sub>2</sub> slant columns (namely the concentration integrated along the effective light path from the sun through the atmosphere to the instrument) are derived using the differential optical absorption spectroscopy (DOAS) method (Platt and Stutz, 2008). The DOAS technique is a least-squares method fitting the molecular absorption cross sections to the measured GOME-2 sun-normalised radiances provided by the EUMETSAT's processing facility. The fit is applied on the data within a fitting window optimised for NO<sub>2</sub>. As analysed by Richter et al. (2011) and in the Quality Assurance for Essential Climate Variables (QA4ECV; <http://www.qa4ecv.eu>) project, extension of the fitting window for GOME-2 increases the signal-to-noise ratio and hence improves the NO<sub>2</sub> slant column error. The total NO<sub>2</sub> slant columns depend on the viewing geometry and also on parameters such as surface albedo and the presence of clouds and aerosol loads. They are therefore converted to initial total NO<sub>2</sub> vertical columns through division by a stratospheric air mass factor.

Second, the stratospheric contribution is estimated and separated from the NO<sub>2</sub> slant columns (referred to as "stratosphere–troposphere separation"). The GDP 4.8 algorithm applies a modified reference sector method, which uses measurements over clean regions to estimate the stratospheric NO<sub>2</sub> columns based on the assumptions of longitudinally invariable stratospheric NO<sub>2</sub> layers and of negligible tropospheric NO<sub>2</sub> abundance over the clean areas. The modified reference sector method defines a global pollution mask to remove potentially polluted regions and applies an interpolation over the unmasked areas to derive the stratospheric NO<sub>2</sub> columns. As a result of using a fixed pollution mask, the modified reference sector method in GDP 4.8 has larger uncertainties over polluted areas, because limited amount of information over continents is used. To overcome the shortcomings, the STRatospheric Estimation Algorithm from Mainz (STREAM) method (Beirle et al., 2016) has been developed for the TROPOMI instrument and was also successfully applied on GOME, SCIAMACHY, OMI, and GOME-2 measurements. Also belonging to the modified reference sector method, STREAM defines not a fixed pollution mask but rather weighting factors for each observation to determine its contribution to the stratospheric estimation.

Third, the tropospheric NO<sub>2</sub> vertical columns are calculated from the tropospheric slant columns by an air mass factor (AMF) calculation, which contributes the largest uncertainty to the NO<sub>2</sub> retrieval, particularly over polluted regions (Boersma et al., 2004). The AMFs are determined with a radiative transfer model (RTM) and stored in a look-up table (LUT) requiring ancillary information such as surface albedo, vertical shape of the a priori NO<sub>2</sub> profile, clouds, and aerosols. Improvements in the RTM and LUT interpolation scheme, the ancillary parameters, and the cloud and

aerosol correction approach have been reported for the OMI instrument (e.g. Boersma et al., 2011; Lorente et al., 2017; Vasilkov et al., 2017; Krotkov et al., 2017; Veeffkind et al., 2016; Lin et al., 2014; Castellanos et al., 2015; Laughner et al., 2018), which in principle are beneficial for similar satellite instruments like GOME-2.

In this paper, a new algorithm to retrieve the total and tropospheric NO<sub>2</sub> for the GOME-2 instruments is described, which includes improvements in each of the three algorithm steps introduced above. The improved algorithm will be implemented in the next version of GDP (referred to as GDP 4.9 hereafter). We briefly introduce the GOME-2 instrument (Sect. 2) and the current operational (GDP 4.8) total and tropospheric NO<sub>2</sub> retrieval algorithm (Sect. 3). We present the improvements to the DOAS slant column retrieval (Sect. 4), the stratosphere–troposphere separation (Sect. 5), and the AMF calculation (Sect. 6). Finally, we show an end-to-end validation of the tropospheric NO<sub>2</sub> dataset using ground-based multiple-axis DOAS (MAXDOAS) datasets with different pollution conditions (Sect. 7).

## 2 Instrument and measurements

GOME-2 is a nadir-scanning UV–VIS spectrometer aboard the MetOp-A and MetOp-B satellites (referred to as GOME-2A and GOME-2B throughout this study) with a satellite repeating cycle of 29 days and an equator crossing time of 19:30 local time (LT) (descending node). The GOME-2 instrument measures the Earth's backscattered radiance and extraterrestrial solar irradiance in the spectral range between 240 and 790 nm. The morning measurements from GOME-2 provide a better understanding of the diurnal variations of the NO<sub>2</sub> columns in combination with afternoon observations from for example the OMI, and TROPOMI instruments (13:30 LT). The default swath width of GOME-2 is 1920 km, enabling a global coverage in  $\sim 1.5$  days. The default ground pixel size is 80 km  $\times$  40 km in the forward scan, which remains almost constant over the full swath width. In a tandem operation of MetOp-A and MetOp-B from July 2013 onwards, a decreased swath of 960 km and an increased spatial resolution of 40 km  $\times$  40 km are employed by GOME-2A. See Munro et al. (2016) for more details on instrument design and performance.

The operational GOME-2 NO<sub>2</sub> product is provided by DLR in the framework of EUMETSAT's Satellite Application Facility on Atmospheric Composition Monitoring (AC-SAF). The product processing chain starts with the level 0 to 1b processing within the core ground segment at EUMETSAT in Darmstadt (Germany), where the raw instrument (level 0) data are converted into geolocated and calibrated (level 1b) (ir)radiances by the GOME-2 Product Processing Facility (PPF). The level 1b (ir)radiances are disseminated through the EUMETCast system to the AC-SAF processing facility at DLR in Oberpfaffenhofen (Germany) and

further processed using the Universal Processor for UV/VIS Atmospheric Spectrometers (UPAS) system. Broadcasted via EUMETCast, WMO GTS, and the Internet, the resulting level 2 near-real-time total column products including NO<sub>2</sub> columns can be received by user communities 2 h after sensing. Offline and reprocessed GOME-2 level 2 and consolidated products are also provided within 1 day by DLR, which can be ordered via FTP server and the EUMETSAT Data Centre (<https://acsaf.org/>, last access: 1 February 2019).

## 3 Total and tropospheric NO<sub>2</sub> retrieval for GDP 4.8

The first main step of the retrieval algorithm is the DOAS technique, which is applied to determine the total NO<sub>2</sub> slant columns from the (ir)radiance spectra measured by the instrument. Based on the Beer–Lambert law, the DOAS fit is a least-squares inversion to isolate the trace gas absorption from the background processes, e.g. extinction resulting from scattering on molecules and aerosols, with a background polynomial  $P(\lambda)$  at wavelength  $\lambda$ :

$$\ln \left[ \frac{I(\lambda) + \text{offset}(\lambda)}{I^0(\lambda)} \right] = - \sum_g S_g \sigma_g(\lambda) - \alpha_R R(\lambda) - P(\lambda). \quad (1)$$

The measurement-based term is defined as the natural logarithm of the measured earthshine radiance spectrum  $I(\lambda)$  divided by the daily solar irradiance spectrum  $I^0(\lambda)$ . The intensity offset correction  $\text{offset}(\lambda)$ , which describes the additional contributions such as stray light in the spectrometer to the measured intensity, is modelled using a zero-order polynomial with the polynomial coefficient as the fitting parameter. The spectral effect from the absorption of species  $g$  is determined by the fitted slant column density  $S_g$  and associated absorption cross section  $\sigma_g(\lambda)$ . An additional term with the Ring scaling factor  $\alpha_R$  and the Ring reference spectrum  $R(\lambda)$  describes the filling-in effect of Fraunhofer lines by rotational Raman scattering (the so-called Ring effect). The GDP 4.8 algorithm adopts a wavelength range of 425–450 nm to ensure prominent NO<sub>2</sub> absorption structures and controllable interferences from other absorbing species, e.g. water vapour (H<sub>2</sub>O<sup>vap</sup>), ozone (O<sub>3</sub>), and oxygen dimer (O<sub>4</sub>). Table 1 gives an overview of the DOAS settings for the current operational GDP 4.8 algorithm, the improved version 4.9 algorithm (see Sect. 4), and the algorithm used in the QA4ECV product (see Sect. 4.5).

The second component in the retrieval is the calculation of initial total vertical column densities  $V_{\text{init}}$  using a stratospheric AMF ( $M_{\text{strat}}$ ) conversion:

$$V_{\text{init}} = \frac{S}{M_{\text{strat}}}. \quad (2)$$

Given the small optical thickness of NO<sub>2</sub>,  $M_{\text{strat}}$  can be determined as

$$M_{\text{strat}} = \frac{\sum_l m_l(\mathbf{b}) x_l c_l}{\sum_l x_l}, \quad (3)$$

**Table 1.** Main settings of GOME-2 DOAS retrieval of NO<sub>2</sub> slant columns discussed in this study.

|                   | GDP 4.8,<br>Valks et al. (2011, 2017)  | GDP 4.9<br>(this work)  | QA4ECV, Müller et al. (2016);<br>Boersma et al. (2018)  |
|-------------------|--|---|---|
| Wavelength range  | 425–450 nm   | 425–497 nm  | 405–465 nm  |
| Cross sections    | NO <sub>2</sub> 240 K, H <sub>2</sub> O <sup>vap</sup> ,<br>O <sub>3</sub> , O <sub>4</sub> , Ring | NO <sub>2</sub> 220 K, H <sub>2</sub> O <sup>vap</sup> , O <sub>3</sub> ,<br>O <sub>4</sub> , Ring, H <sub>2</sub> O <sup>liq</sup> , Eta,<br>Zeta, resolution correction | NO <sub>2</sub> 220 K, H <sub>2</sub> O <sup>vap</sup> , O <sub>3</sub> , O <sub>4</sub> ,<br>Ring, H <sub>2</sub> O <sup>liq</sup> |
| Polynomial degree | 3  | 5   | 5   |
| Intensity offset  | Constant   | Linear  | Constant  |
| Slit function     | Preflight  | Stretched preflight   | Preflight   |

with  $m_l$  the box-air-mass factors (box-AMFs) in layer  $l$ ,  $x_l$  the altitude-dependent sub-columns from a stratospheric a priori NO<sub>2</sub> profiles climatology (Lambert et al., 1999), and  $c_l$  a correction coefficient to account for the temperature dependency of NO<sub>2</sub> cross section (Boersma et al., 2004; Nüß et al., 2006). The calculation of  $V_{\text{init}}$  assumes negligible tropospheric NO<sub>2</sub> and hence uses only the stratospheric a priori NO<sub>2</sub> profiles to derive AMF. The box-AMFs  $m_l$  are derived using the multilayered multiple scattering LInearized Discrete Ordinate Radiative Transfer (LIDORT) RTM (Spurr et al., 2001) and stored in a LUT as a function of various model inputs  $\mathbf{b}$ , including GOME-2 viewing geometry, surface pressure, and surface albedo. The surface albedo is described by the Lambertian equivalent reflectivity (LER). The surface LER climatology used in the GDP 4.8 algorithm is derived from combined TOMS–GOME measurements (Boersma et al., 2004) for the years 1979–1993 with a spatial resolution of 1.25° long. × 1.0° lat.

In the presence of clouds, the calculation of  $M_{\text{strat}}$  adopts the independent pixel approximation based on GOME-2 cloud parameters:

$$M_{\text{strat}} = \omega M_{\text{strat}}^{\text{cloud}} + (1 - \omega) M_{\text{strat}}^{\text{clear}}, \quad (4)$$

with  $\omega$  being the cloud radiance fraction,  $M_{\text{strat}}^{\text{cloud}}$  the cloudy-sky stratospheric AMF, and  $M_{\text{strat}}^{\text{clear}}$  the clear-sky stratospheric AMF.  $M_{\text{strat}}^{\text{cloud}}$  and  $M_{\text{strat}}^{\text{clear}}$  are derived with Eq. (3) with  $M_{\text{strat}}^{\text{cloud}}$  mainly relying on the cloud pressure and the cloud albedo. The  $\omega$  value is derived from the cloud fraction  $c_f$ :

$$\omega = \frac{c_f I^{\text{cloud}}}{(1 - c_f) I^{\text{clear}} + c_f I^{\text{cloud}}}, \quad (5)$$

where  $I^{\text{cloud}}$  is the radiance for a cloudy scene and  $I^{\text{clear}}$  for a clear scene.  $I^{\text{cloud}}$  and  $I^{\text{clear}}$  are calculated using LIDORT, depending mostly on the GOME-2 viewing geometry, surface albedo, and cloud albedo. From GOME-2,  $c_f$  is determined with the Optical Cloud Recognition Algorithm (OCRA) by separating a spectral scene into cloudy contribution and cloud-free background, and the cloud pressure and the cloud albedo are derived using the Retrieval Of Cloud Information using Neural Networks (ROCINN) algorithm by comparing simulated and measured radiance in and near the

O<sub>2</sub> A band (Loyola et al., 2007, 2011). Applied in the NO<sub>2</sub> retrieval in GDP 4.8, the latest version 3.0 of the OCRA (Lutz et al., 2016) applies a degradation correction on the GOME-2 level 1 measurements as well as corrections for viewing angle and latitudinal dependencies. A new cloud-free background is constructed from 6 years of GOME-2A measurements from the years 2008–2013. The updated OCRA also includes an improved detection and removal of sun glint that affects most of the GOME-2 orbits. Version 3.0 of ROCINN (Loyola et al., 2018) applies a forward RTM calculation using updated surface albedo climatology and spectroscopic data as well as a new inversion scheme based on Tikhonov regularisation (Tikhonov and Arsenin, 1977; Doicu et al., 2010). The computation time of ROCINN is optimised with a smart sampling method (Loyola et al., 2016).

The next retrieval step is the separation of stratospheric and tropospheric components from the initial vertical total columns, namely the stratosphere–troposphere separation. Since no direct stratospheric measurements are available for GOME-2, a spatial filtering algorithm is applied to estimate the stratospheric NO<sub>2</sub> columns in GDP 4.8. The spatial filtering algorithm belongs to the modified reference sector method, which uses total NO<sub>2</sub> columns over clean regions to approximate the stratospheric NO<sub>2</sub> columns based on the assumption of longitudinally invariable stratospheric NO<sub>2</sub> layers and of negligible tropospheric NO<sub>2</sub> abundance over the clean areas. The spatial filtering algorithm uses a pollution mask to filter the potentially polluted areas (tropospheric NO<sub>2</sub> columns larger than  $1 \times 10^{15}$  molec cm<sup>2</sup>), followed by a low-pass filtering (with a zonal 30° boxcar filter) on the initial total columns of the unmasked areas, and afterwards a removal of a tropospheric background NO<sub>2</sub> ( $1 \times 10^{14}$  molec cm<sup>2</sup>) from the derived stratospheric columns.

Finally, the tropospheric NO<sub>2</sub> columns  $V_{\text{trop}}$  can be computed as

$$V_{\text{trop}} = \frac{M_{\text{strat}}}{M_{\text{trop}}} \times T, \quad (6)$$

where  $M_{\text{strat}}$  is the stratospheric AMF in Eq. (3),  $M_{\text{trop}}$  is the tropospheric AMF, and  $T$  is the tropospheric residues ( $T = V_{\text{init}} - V_{\text{strat}}$ ).  $M_{\text{trop}}$  is determined using Eqs. (3) and (4) with tropospheric a priori NO<sub>2</sub> profiles. The calculation of  $M_{\text{trop}}$

relies on the same model parameters as of  $M_{\text{strat}}$ , but the dependency on the parameters like surface albedo and cloud properties as well as on the a priori NO<sub>2</sub> profiles is much stronger. The GDP 4.8 adopts the tropospheric a priori NO<sub>2</sub> profiles from a run of the global chemistry transport model MOZART version 2 (Horowitz et al., 2003) with anthropogenic emissions from the EDGAR2.0 inventory (Olivier et al., 1996) for the early 1990s. The monthly average vertical profiles are calculated from MOZART-2 data from the year 1997 for the overpass time of GOME-2 (09:30 LT) with a resolution of 1.875° long × 1.875° lat.

#### 4 Improved DOAS slant column retrieval

A larger 425–497 nm wavelength fitting window for the DOAS method (Richter et al., 2011) is implemented in the GDP 4.9 to retrieve the NO<sub>2</sub> slant columns, which improves the signal-to-noise ratio by including more NO<sub>2</sub> absorption structures. Compared to the extended 405–465 nm range, as employed by the QA4ECV GOME-2 NO<sub>2</sub> product and used in the NO<sub>2</sub> retrieval for OMI instrument (Boersma et al., 2002; van Geffen et al., 2015), the 425–497 nm fitting window has stronger sensitivity to NO<sub>2</sub> columns in the boundary layer because the importance of scattering decreases with wavelength (Richter and verification team, 2015). In this study, the slant columns are derived using QDOAS software developed at the Belgian Institute for Space Aeronomy (BIRA-IASB) (Danckaert et al., 2015)<sup>1</sup>. Table 1 summarises the new settings of the GDP 4.9 algorithm.

##### 4.1 Absorption cross sections

In the fitting window optimised for NO<sub>2</sub> retrieval, the DOAS fit includes species with strong and unique absorption structures and describes their spectral effect using absorption cross sections from literature. In our GDP 4.9 algorithm, the absorption cross sections of NO<sub>2</sub>, H<sub>2</sub>O<sup>vap</sup>, O<sub>3</sub>, and O<sub>4</sub> are updated mainly with newly released datasets as

- NO<sub>2</sub> absorption at 220 K from Vandaele et al. (2002);
- O<sub>3</sub> absorption at 228 K from Brion et al. (1998);
- H<sub>2</sub>O<sup>vap</sup> absorption at 293 K from HITEMP (Rothman et al., 2010), rescaled as in Lampel et al. (2015);
- O<sub>4</sub> absorption at 293 K from Thalman and Volkamer (2013).

In addition, to compensate for the larger spectral interference from liquid water (H<sub>2</sub>O<sup>liq</sup>), a H<sub>2</sub>O<sup>liq</sup> absorption (Pope and Fry, 1997) is included to reduce systematic errors above ocean for the wider wavelength range. Two additional GOME-2 polarisation key data (EUMETSAT, 2009)

<sup>1</sup>Note that the derived slant columns are scaled by geometric AMFs to correct for the angular dependencies of GOME-2 measurements in this section.

are included to correct for remaining polarisation correction problems, particularly for GOME-2B:

- H<sub>2</sub>O<sup>liq</sup> absorption at 297 K from Pope and Fry (1997), smoothed as in Peters et al. (2014);
- Eta and Zeta from GOME-2 calibration key data (EUMETSAT, 2009).

It is worth noting that our improved DOAS retrieval in the GDP 4.9 adopts a decreased temperature of NO<sub>2</sub> cross section (220 instead of 240 K in GDP 4.8; Valks et al., 2017) for a consistency with other NO<sub>2</sub> retrievals from GOME-2, OMI, and TROPOMI (Müller et al., 2016; Boersma et al., 2002; van Geffen et al., 2015, 2016), with a minor effect on the fit quality (~ 0.02 %) from the two temperatures. Changing the temperature of the NO<sub>2</sub> cross section from 240 to 220 K reduces the NO<sub>2</sub> slant columns by ~ 6 %–9 %, but this temperature dependency is corrected in the AMF and vertical column calculation (see Eq. 3).

The spectral signature of sand absorption has been investigated by Richter et al. (2011) for GOME-2 data, but it is not applied here because of the potential interference with the broadband liquid water structure (Peters et al., 2014), which might lead to non-physical results over the ocean.

##### 4.2 Intensity offset correction

Besides the radiances backscattered by the Earth's atmosphere, a number of both natural (i.e. the Ring effect) and instrumental (e.g. stray light in the spectrometer and change of detector's dark current) sources contribute to an additional "offset" to the scattering intensity. To correct for this drift, an intensity offset correction with a linear wavelength dependency (i.e. polynomial degree of 1) is applied for the large fitting window in this study. Figure 1 illustrates the effect of using a linear intensity offset correction for the large fitting window on 3 March 2008. The use of a linear offset correction increases the NO<sub>2</sub> columns by up to 3 × 10<sup>14</sup> molec cm<sup>2</sup> (17 %) and decreases the fitting residues (retrieval root mean square, rms) by up to 30 %. Larger differences are found at the eastern scans (eastern part of GOME-2 swath), possibly suggesting instrumental issues specific to GOME-2. For the retrieval rms, stronger improvements are mainly located above ocean, arguably from the compensation of inelastic vibrational Raman scattering in water bodies (Vountas et al., 2003).

The intensity offset can also be fitted using only the constant term, as employed by the GDP 4.8 algorithm (with 425–450 nm wavelength window) and as recommended by the QA4ECV algorithm (with 405–465 nm). Compared to the use of the linear intensity offset correction, the application of a constant term on our retrieval shows a decrease in the NO<sub>2</sub> columns by up to 3.5 × 10<sup>14</sup> molec cm<sup>2</sup> (17 %) and an increase in the retrieval rms by up to 14 %, which implies the necessity of using a linear intensity offset correction for the large 425–497 nm wavelength range.

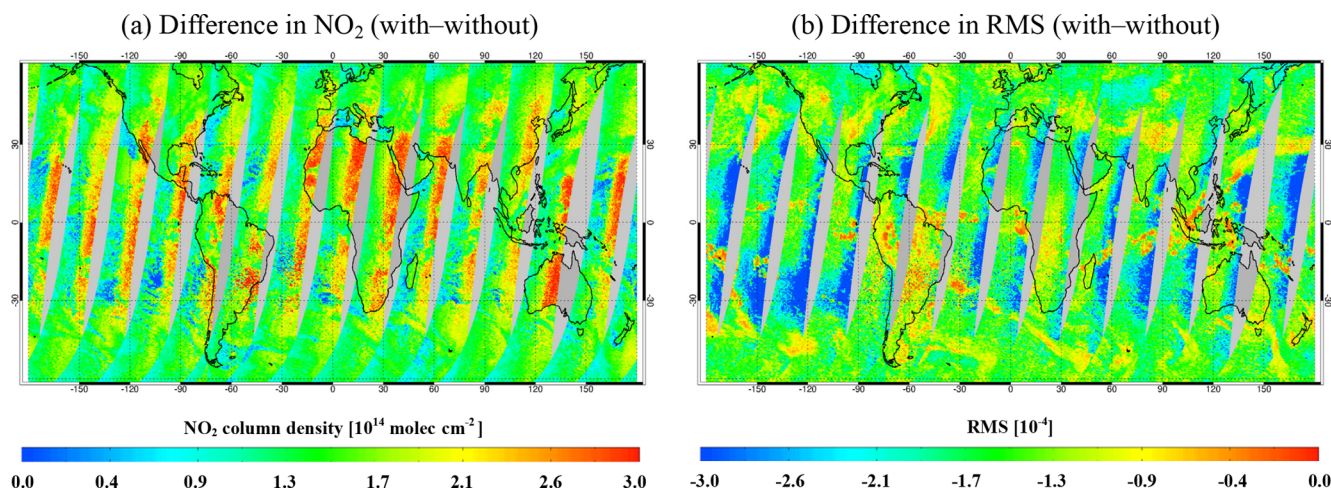


**Figure 1.** Difference in NO<sub>2</sub> columns (slant columns scaled by geometric AMFs) (a) and retrieval rms (b) estimated with and without a linear intensity offset correction for GOME-2A on 3 March 2008.

### 4.3 GOME-2 slit function treatment

An accurate treatment of the instrumental slit function is essential for the wavelength calibration and the convolution of high-resolution laboratory cross sections. In spite of a generally good spectral stability of GOME-2 in orbit, the width of GOME-2 slit function has been changing on both long and short timescales (Munro et al., 2016), which needs to be accounted for in the DOAS analysis. In this study, an improved treatment of GOME-2 slit function in the DOAS fit is achieved by calculating effective slit functions from GOME-2 irradiance measurements to correct for the long-term variations (see Sect. 4.3.1) and by including an additional cross section in the DOAS fit to correct for the short-term variations (see Sect. 4.3.2).

#### 4.3.1 Long-term variations

To analyse the long-term variations of the GOME-2 instrumental slit function and the impact on our retrieval, effective slit functions are derived by convolving a high-resolution reference solar spectrum (Chance and Kurucz, 2010) with a stretched preflight GOME-2 slit function and aligning to the GOME-2 daily irradiance measurements with stretch factors as fit parameters. The effective slit functions are calculated in 13 sub-windows covering the full fitting window (425–497 nm). Figure 2 displays the long-term evolution of the fitted GOME-2 slit function width (full width at half maximum, FWHM) calculated from the stretch factors. The GOME-2 slit function has narrowed after the launch by  $\sim 5\%$  for GOME-2A and  $\sim 3.5\%$  for GOME-2B at 451 nm, in agreement with Dikty et al. (2011), Azam et al. (2015), and Munro et al. (2016). For GOME-2A, visible discontinuities of the slit function width are related to the in-orbit instrument operations, including an apparent anomaly in September 2009 when a major throughput test was performed (EUMETSAT,

2012). After the throughput test, the narrowing of the slit function slowed down. For GOME-2B, stronger seasonal fluctuations of the FWHM are found. The seasonal and long-term variations in the GOME-2 slit function are caused by changing temperatures of the optical bench due to the seasonal variation in solar heating and the lack of thermal stability of the optical bench, respectively (Munro et al., 2016). Although the variations are only a few percent, the effect on the DOAS retrieval is significant. Compared to the application of the preflight slit function, the use of a stretched slit function improves the calibration residuals by  $\sim 40\%$  for both GOME-2A and GOME-2B (not shown).

In previous studies, slit functions have also been fitted using various Gaussian shapes. For instance, De Smedt et al. (2012) have derived effective GOME-2 slit functions for formaldehyde retrieval using an asymmetric Gaussian with its width and shape as fit parameters. For NO<sub>2</sub> retrieval, the use of effective slit functions with an asymmetric Gaussian leads to similar results as using a preflight slit function. In addition, Beirle et al. (2017) have proposed a slit function parameterisation using a super Gaussian, which is proved to quickly and robustly describe the slit function changes for satellite instrument OMI or TROPOMI. In the case of GOME-2, the super Gaussian obtains nearly identical results as the asymmetric Gaussian and is therefore not applied in here.

#### 4.3.2 In-orbit variations

To correct for the in-orbit variations of GOME-2 slit function, a “resolution correction function” (Azam et al., 2015) is included as an additional cross section in the DOAS fit (see Table 1). The cross section is derived by dividing a high-resolution solar spectrum (Chance and Kurucz, 2010) convolved with a stretched preflight GOME-2 slit function (see

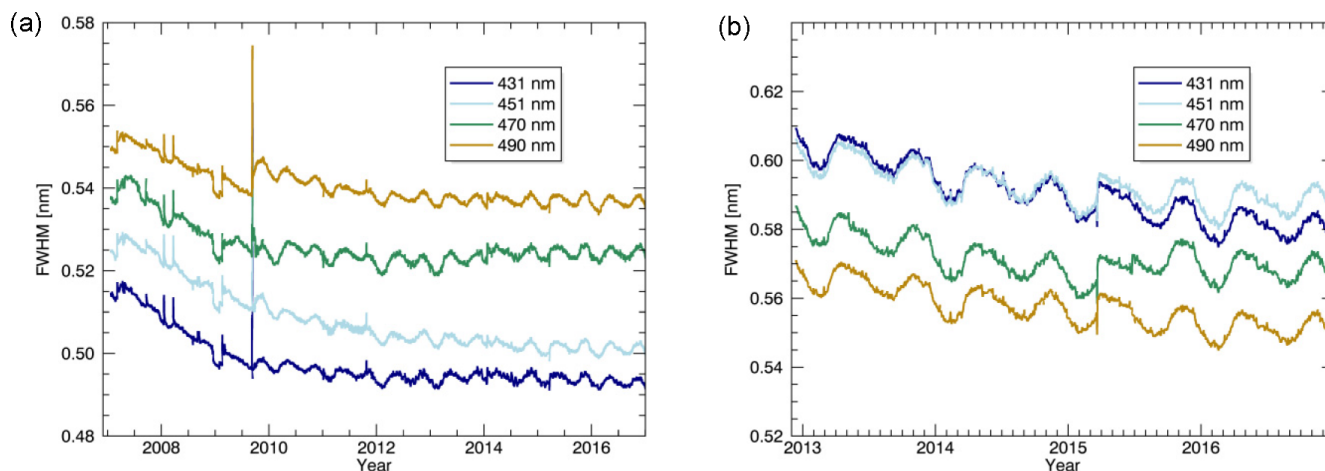


**Figure 2.** Temporal evolution of the fitted slit function FWHM for GOME-2A (a, January 2007–December 2016) and GOME-2B (b, December 2012–December 2016.)

Sect. 4.3.1) by itself but convolved with a slightly modified slit function. Figure 3 shows an example of the fit coefficients and the influence on our DOAS retrieval on 1 February 2013. As shown in the left panel, the slit function width increases along the orbit by  $\sim 2 \times 10^{-3}$  nm ( $\sim 0.4\%$ ) for GOME-2A (see Beirle et al., 2017, Fig. 8 therein) and  $\sim 5.2 \times 10^{-3}$  nm ( $\sim 1\%$ ) for GOME-2B (a fit coefficient of  $1 \times 10^{-2}$  corresponds to a change in the slit function width of  $\sim 2.8 \times 10^{-3}$  nm). This in-orbit broadening of the slit function is caused by the increasing temperature of the instrument along the orbit. Taking into account the in-orbit broadening in the DOAS fit decreases the retrieval rms by up to 5% for GOME-2A and up to 12% for GOME-2B in Fig. 3b.

#### 4.4 GOME-2 level 1b data

As described in Sect. 2, the level 0 to 1b processing by the PPF at EUMETSAT calculates the geolocation and calibration parameters and produces the calibrated level 1b (ir)radiance. Due to the incomplete removal of Xe-line contamination in the GOME-2B calibration key data (calibration key data are taken during the on-ground campaign and required as an input to the level 0 to 1b processing), artefacts at wavelengths larger than 460 nm have been reported by Azam et al. (2015) for GOME-2B irradiances. Mainly focusing on the cleaning of contamination in the GOME-2B calibration key data, a new 6.1 version of the GOME-2 level 0 to 1b processor has been activated from 25 June 2015 onwards (EUMETSAT, 2015). To study the impact of the new level 1b data on our GDP 4.9 algorithm using the 425–497 nm fitting window, the retrieval is analysed using both the new 6.1 version (testing dataset provided by EUMETSAT for March 2015) and the previous version 6.0 data for the same period. Figure 4 presents a comparison of the retrieved NO<sub>2</sub> columns over the Pacific for GOME-2A and GOME-2B. The application of the version 6.1 level 1b data slightly reduces the

NO<sub>2</sub> columns by  $\sim 1\text{--}1.5 \times 10^{14}$  molec cm<sup>2</sup> ( $\sim 6\%\text{--}11\%$ ) for GOME-2A. A larger effect is observed for GOME-2B with a decrease of NO<sub>2</sub> columns by  $\sim 3\text{--}4 \times 10^{14}$  molec cm<sup>2</sup> ( $\sim 15\%\text{--}23\%$ ) and a reduction of rms error by  $\sim 27\%\text{--}33\%$  (not shown). The stronger decrease of GOME-2B NO<sub>2</sub> columns leads to a better consistency between the datasets from GOME-2A and GOME-2B with an overall bias reduced from  $\sim 3 \times 10^{14}$  molec cm<sup>2</sup> to  $\sim 1 \times 10^{14}$  molec cm<sup>2</sup>.

#### 4.5 Comparison to QA4ECV data

The quality of the GDP 4.9 retrieval is evaluated using the GOME-2 NO<sub>2</sub> dataset from QA4ECV, which is a project aiming at quality-assured satellite products using a retrieval algorithm harmonised for GOME, SCIAMACHY, OMI and GOME-2. The GOME-2A NO<sub>2</sub> columns from QA4ECV (version 1.1) for the years 2007–2015 have shown an improved quality over previous datasets (Zara et al., 2018). Table 1 gives an overview of the DOAS settings used in the QA4ECV project. Figure 5 shows a comparison of the NO<sub>2</sub> columns over the Pacific from the GDP 4.8 algorithm, the GDP 4.9 algorithm, and the QA4ECV data for February 2007. For comparison, only ground pixels with a solar zenith angle smaller than 80° are considered. The GDP 4.8 dataset has been adjusted using a 220 K (Vandaele et al., 2002) NO<sub>2</sub> cross section to remove the influence of temperature dependency of the NO<sub>2</sub> cross section (see discussion in Sect. 4.1). Compared to the GDP 4.8 dataset, the improved DOAS retrieval in GDP 4.9 increases the NO<sub>2</sub> columns by  $\sim 1\text{--}3 \times 10^{14}$  molec cm<sup>2</sup> (up to 27%). Compared to the QA4ECV product, a good overall consistency is found with the GDP 4.9 dataset at all latitudes considering the different DOAS settings such as fitting window, offset correction, and slit function characterisation.

Figure 6 presents the time series of calculated slant column errors from the three datasets, following a statistical method

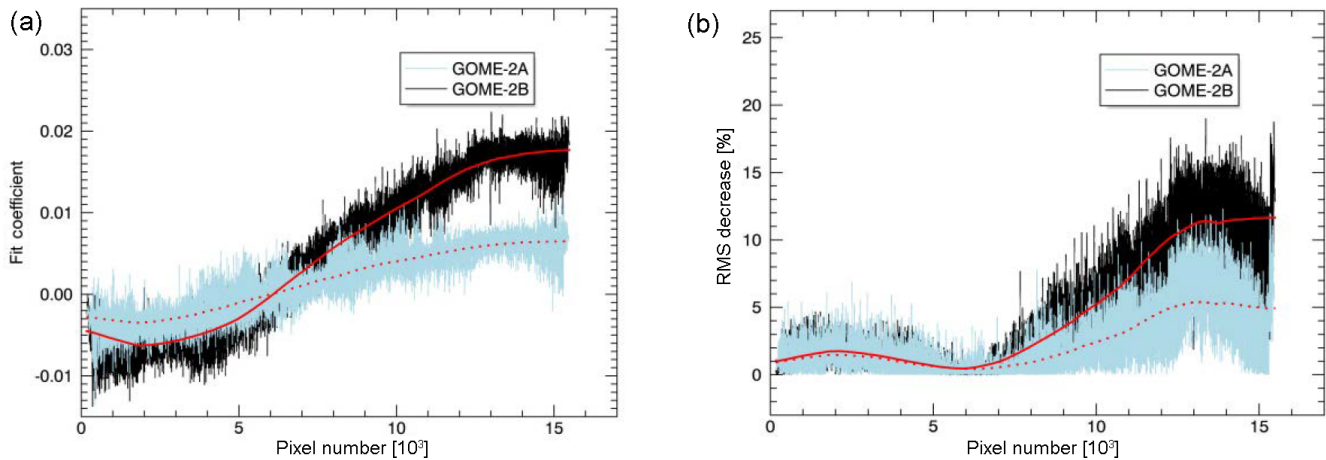


**Figure 3.** Changes of GOME-2 slit function width along orbit 32 636 on 1 February 2013 (a) and the impact on the retrieval rms error (b). Red lines provide the boxcar average for GOME-2A (dotted) and GOME-2B (solid). A fit coefficient of  $1 \times 10^{-2}$  corresponds to a change in the slit function width of  $\sim 2.8 \times 10^{-3}$  nm (a).

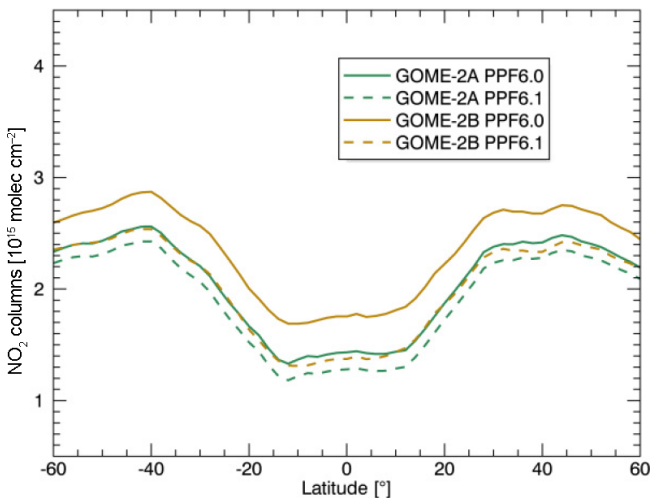


**Figure 4.** Monthly zonal average NO<sub>2</sub> columns (slant columns scaled by geometric AMFs) for GOME-2A (green) and GOME-2B (brown) using the new PPF 6.1 (dotted) and PPF 6.0 (solid) data in March 2015 over the Pacific (160–180° E).

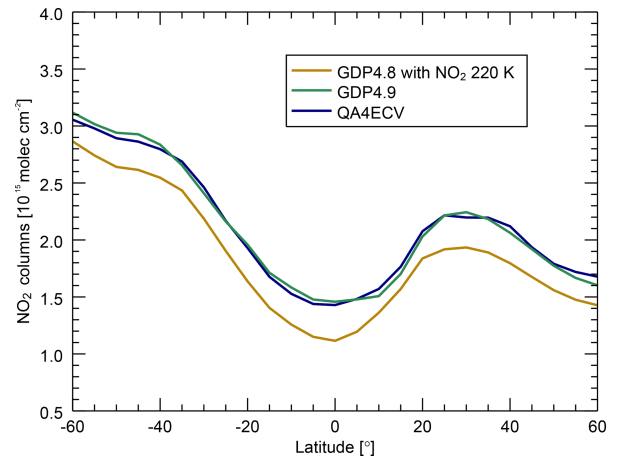


**Figure 5.** Comparisons of monthly zonal average NO<sub>2</sub> columns (slant columns scaled by geometric AMFs) from the operational GDP 4.8 product (but retrieved using a 220 K NO<sub>2</sub> cross section from Vandaele et al., 2002) (brown), the improved GDP 4.9 algorithm (green), and the QA4ECV dataset (blue) over the Pacific (160–180° E) in February 2007 for GOME-2A.

to analyse the NO<sub>2</sub> slant column uncertainty for GOME-2 (Valks et al., 2011, Sect. 6.1 therein). The slant column errors, calculated as variations of NO<sub>2</sub> measurements within small boxes ( $2^\circ \times 2^\circ$ ) over the tropical Pacific ( $20^\circ\text{S}$ – $20^\circ\text{N}$ ,  $160$ – $180^\circ\text{E}$ ), increase for all the three datasets as a result of instrument degradation (Dikty et al., 2011; Munro et al., 2016) until the major throughput test in September 2009 (see Sect. 4.3.1) and stabilise afterwards. Mainly driven by the use of a wider fitting window with stronger absorptions, the smallest slant column errors are found by the GDP 4.9 algorithm, e.g. 23.8 % smaller than from the GDP 4.8 and 13.5 % smaller than from the QA4ECV dataset in February 2007,

with an increasing difference with time for the QA4ECV dataset (27.9 % in December 2015).

## 5 New stratosphere–troposphere separation

The calculation of tropospheric NO<sub>2</sub> requires an estimation and removal of the stratospheric contribution to the initial total NO<sub>2</sub> columns. In our GDP 4.9 retrieval, the stratosphere–troposphere separation algorithm STREAM (Beirle et al., 2016) has been adapted to GOME-2 measurements. Belonging to the modified reference sector method, STREAM uses initial total NO<sub>2</sub> columns with negligible tropospheric

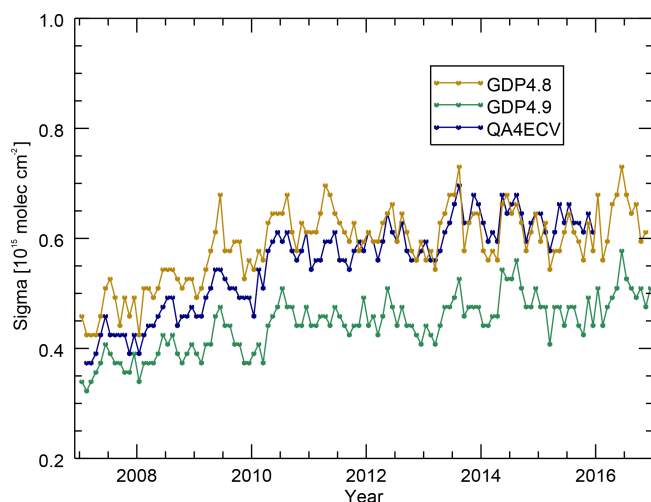


**Figure 6.** Temporal evolution of the NO<sub>2</sub> slant column errors from the operational GDP 4.8 product (brown, January 2007–December 2016), the improved GDP 4.9 algorithm (green, January 2007–December 2016), and the QA4ECV dataset (blue, February 2007–December 2015) for GOME-2A, using deviations of NO<sub>2</sub> slant columns from box ( $2^\circ \times 2^\circ$ ) mean values over the tropical Pacific ( $20^\circ \text{S}$ – $20^\circ \text{N}$ ,  $160$ – $180^\circ \text{E}$ ).

contribution, i.e. unpolluted measurements at remote areas and cloudy measurements at medium altitudes, to derive the stratospheric NO<sub>2</sub> columns. Based on a tropospheric NO<sub>2</sub> climatology and the GOME-2 cloud product, STREAM calculates weighting factors for each satellite pixel to define the contribution of initial total columns to the stratospheric estimation; potentially polluted pixels are weighted low instead of being totally masked out in the GDP 4.8 spatial filtering method, cloudy observations at medium altitudes are given higher weights because they directly provide the stratospheric information, and the weights are further adjusted in a second iteration if pixels suffer from large biases in the tropospheric residues. Depending on these weighting factors, stratospheric NO<sub>2</sub> fields are derived by weighted convolution on the daily initial total columns using convolution kernels. The convolution kernels are wider at lower latitudes due to the longitudinal homogeneity assumption of stratospheric NO<sub>2</sub> and narrower at higher latitudes to reflect the stronger natural variations. To remove the biases in the weighted convolution resulting from the large latitudinal gradients, a latitudinal correction is applied on the initial total columns: the latitudinal dependencies of initial total NO<sub>2</sub> are calculated over the clean Pacific, removed from the initial total NO<sub>2</sub> before weighted convolution, and added back to the estimated stratospheric columns afterwards. However, we found that longitudinal variations of NO<sub>2</sub> concentration resulted in biases in the latitudinal correction and hence in the stratospheric estimation. For the adaptation of STREAM to GOME-2 measurements, the performance of STREAM is analysed using synthetic GOME-2 NO<sub>2</sub> observations (see

Sect. 5.1), and an improved latitudinal correction is applied (see Sect. 5.2).

## 5.1 Performance of STREAM

To test the performance of STREAM for GOME-2, simulated NO<sub>2</sub> fields from the C-IFS-CB05-BASCOE (referred to as C-IFS throughout this work) experiment (Huijnen et al., 2016) are applied. The C-IFS model is a combination of tropospheric chemistry module in the Integrated Forecast System (IFS, with current version based on the Carbon Bond chemistry scheme, CB05) of the European Centre for Medium-Range Weather Forecasts (ECMWF) and stratospheric chemistry from the Belgian Assimilation System for Chemical Observations (BASCOE) system. Based on 1 year of C-IFS data (2009) at a resolution of  $0.75^\circ \text{ long.} \times 0.75^\circ \text{ lat.}$ , synthetic initial total columns  $V_{\text{init}}$  are calculated as

$$V_{\text{init}} = \frac{S}{M_{\text{strat}}} = \frac{V_{\text{total}} \times M_{\text{total}}}{M_{\text{strat}}} \quad (7)$$

(see Eq. 2). Modelled NO<sub>2</sub> slant columns  $S$  are based on the total vertical columns  $V_{\text{total}}$  from C-IFS with interpolation to match the GOME-2 centre pixel coordinate and measurement time. Total AMFs  $M_{\text{total}}$  and stratospheric AMFs  $M_{\text{strat}}$  are derived using Eqs. (3)–(5) with surface properties and cloud information from GOME-2 orbital data and with C-IFS a priori NO<sub>2</sub> profiles for the whole atmosphere and between the tropopause (defined by a latitude-dependent parameterisation with the tropopause height ranging from 270 hPa for arctic to 92 hPa for tropics) and the top of the atmosphere, respectively. The performance of STREAM is evaluated by applying the synthetic initial total NO<sub>2</sub> columns and comparing the estimated stratospheric NO<sub>2</sub> columns with the a priori truth (stratospheric fields from C-IFS integrated between the tropopause and the top of the atmosphere).

Figure 7 displays the synthetic initial total columns from C-IFS, the modelled stratospheric columns, and the estimated stratospheric columns from STREAM on 5 February and 5 August 2009. The result from STREAM presents an overall smooth stratospheric pattern with a strong latitudinal and seasonal dependency resulting from photochemical changes and dynamical variabilities. Because the stratospheric values over polluted regions are taken from the clean measurements at the same latitude, the stratospheric and tropospheric contribution over polluted regions is well separated by STREAM, especially in the Northern Hemisphere. Due to the latitude-dependent definition of convolution kernels, STREAM conserves the longitudinal gradients of stratospheric NO<sub>2</sub> at low latitudes and identifies certain strong stratospheric variations at high latitudes, e.g. in the polar vortex on 5 February. However, smaller structures in the synthetic initial total columns, for instance, resulting from the diurnal variation of NO<sub>2</sub> across an orbital swath,

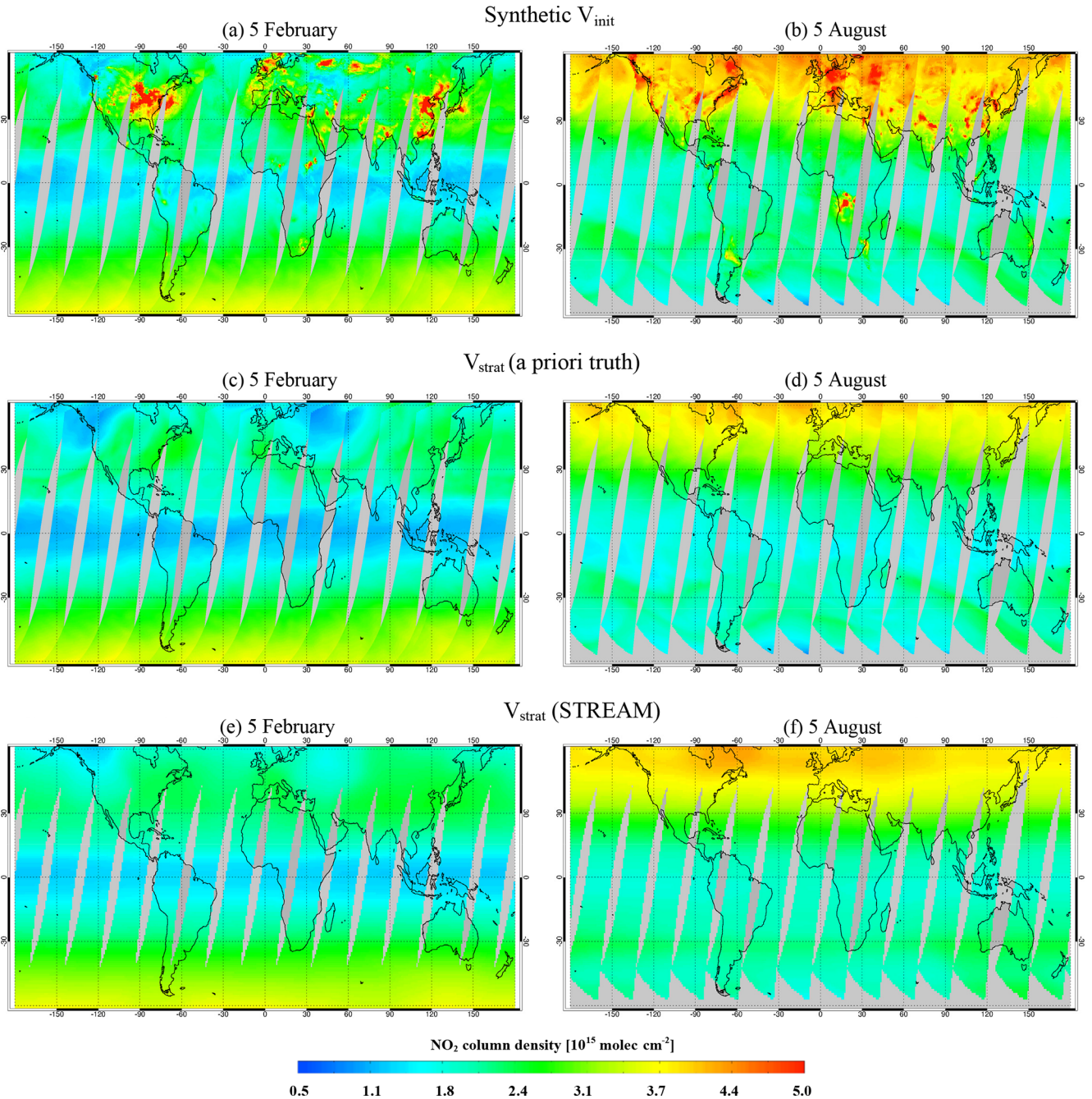


**Figure 7.** Synthetic initial total NO<sub>2</sub> columns (a, b), a priori stratospheric columns from C-IFS (c, d), and estimated stratospheric columns from STREAM (e, f) on 5 February (a, c, e) and 5 August (b, d, f) 2009.

are aliased into the troposphere by STREAM due to the use of convolution kernels.

Figure 8a, b shows the differences in estimated (Fig. 7e, f) and a priori (Fig. 7c, d) stratospheric NO<sub>2</sub>. Overall, the stratospheric columns estimated from STREAM show good agreement with the modelled truth with a slight overestimation, e.g. by  $\sim 1\text{--}2 \times 10^{14}$  molec cm<sup>-2</sup> over low latitudes for both days. Larger differences are found at higher latitudes,

especially in winter, e.g. by  $\sim 5 \times 10^{14}$  molec cm<sup>-2</sup> over eastern Europe and over the North Pacific (west of Canada) on 5 February. The strong longitudinal variations of NO<sub>2</sub> over these regions in the a priori truth (Fig. 7c, d) can not be completely captured by STREAM (Fig. 7e, f), which is a general limitation of the modified reference sector method. Note that these larger differences are reduced to  $\sim 2 \times 10^{14}$  molec cm<sup>-2</sup> in monthly averages (not shown). The found deviations are

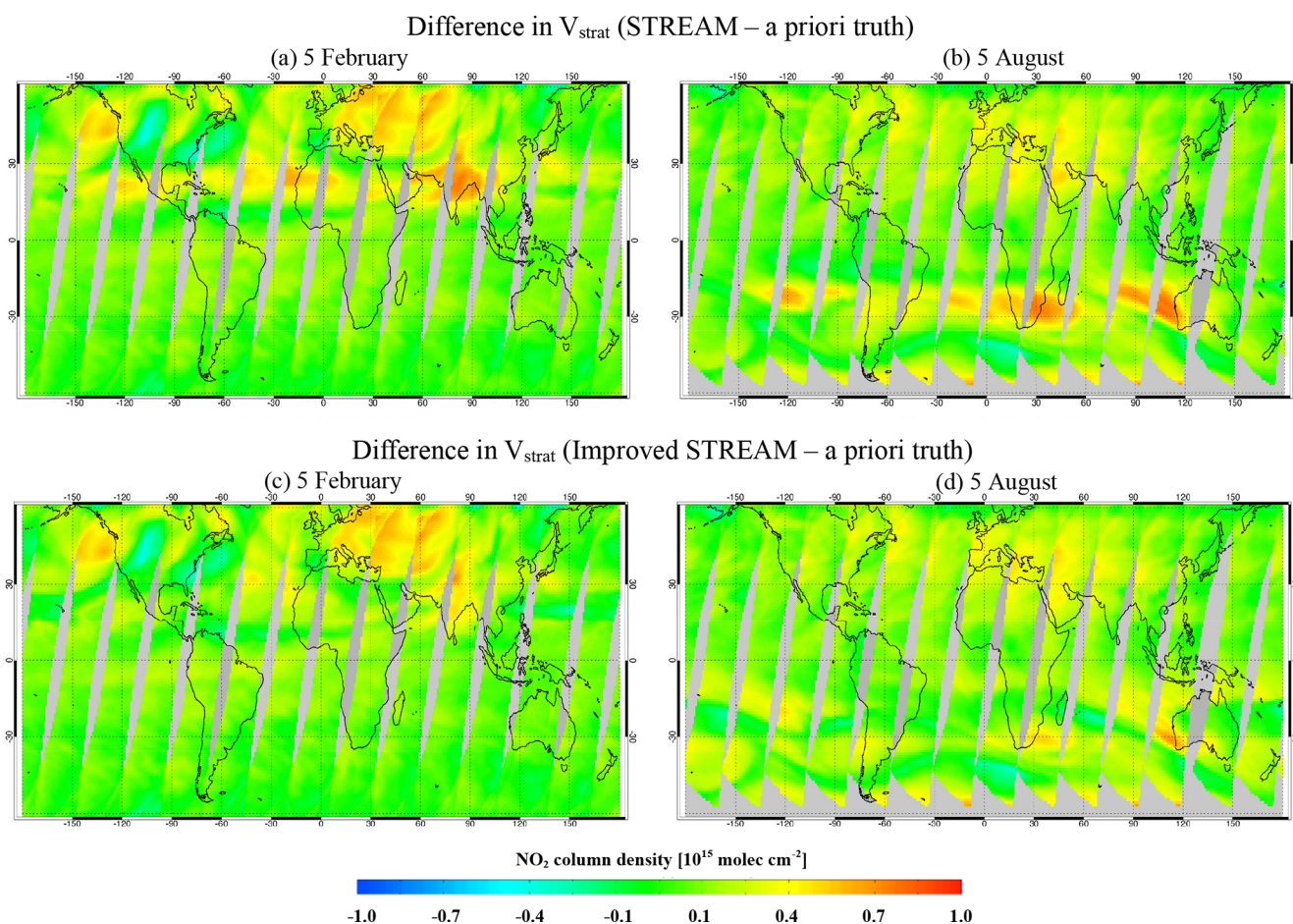


**Figure 8.** Difference in the stratospheric NO<sub>2</sub> columns estimated from STREAM and modelled by C-IFS on 5 February (a) and 5 August (b) 2009. Panels (c) and (d) show STREAM with improved latitudinal correction.

in agreement with the uncertainty estimates in Beirle et al. (2016).

## 5.2 Improved latitudinal correction

In Fig. 8a, b, larger differences are noticeable over the subtropical regions in winter for both days, primarily related to the latitudinal correction used in STREAM. As described in the previous Sect. 5, the latitudinal correction is applied by determining the latitudinal dependencies of total NO<sub>2</sub> over the clean Pacific, removing the latitudinal dependencies before convolution and adding it back to the estimated stratospheric columns. However, longitudinal variations of total NO<sub>2</sub>, for instance, enhanced total NO<sub>2</sub> columns over the Pacific (compared to the Atlantic Ocean) at 15–30° N on 5 February 2009 (Fig. 7a), introduce biases in the stratospheric NO<sub>2</sub> columns. Therefore, an improved latitudinal correction is introduced to reduce the biases over the subtropics. The new latitudinal correction determines the latitudinal dependencies of total NO<sub>2</sub> based on clean measurements in the whole latitude band (the median of lowest NO<sub>2</sub> columns

for each 1° latitude band). Figure 8c, d shows the difference for the estimated stratospheric NO<sub>2</sub> using the improved latitudinal correction. For both days, the application of the new latitudinal correction in STREAM largely removes the biases over the subtropics in Fig. 8a, b.

Applying the improved STREAM on GOME-2 data, Fig. 9 presents the initial total columns from GOME-2 and the stratospheric NO<sub>2</sub> calculated with STREAM and with the spatial filtering method used in the GDP 4.8 algorithm (see Sect. 3) in February and August 2009. For both months, the results calculated with STREAM and with the spatial filtering method show similar global structures. Since the spatial filtering method applies a fixed pollution mask to remove the potentially polluted regions (tropospheric NO<sub>2</sub> larger than  $1 \times 10^{15}$  molec cm<sup>-2</sup>), moderately polluted pixels with tropospheric NO<sub>2</sub> up to  $1 \times 10^{15}$  molec cm<sup>-2</sup> still contribute to the stratospheric estimation. Therefore, enhanced stratospheric NO<sub>2</sub> by more than  $5 \times 10^{14}$  molec cm<sup>-2</sup> is found over polluted regions, e.g. the Middle East, China, central Africa, southern Africa, and Australia in Fig. 9e, f. This overestimation is largely removed by STREAM in Fig. 9c, d.

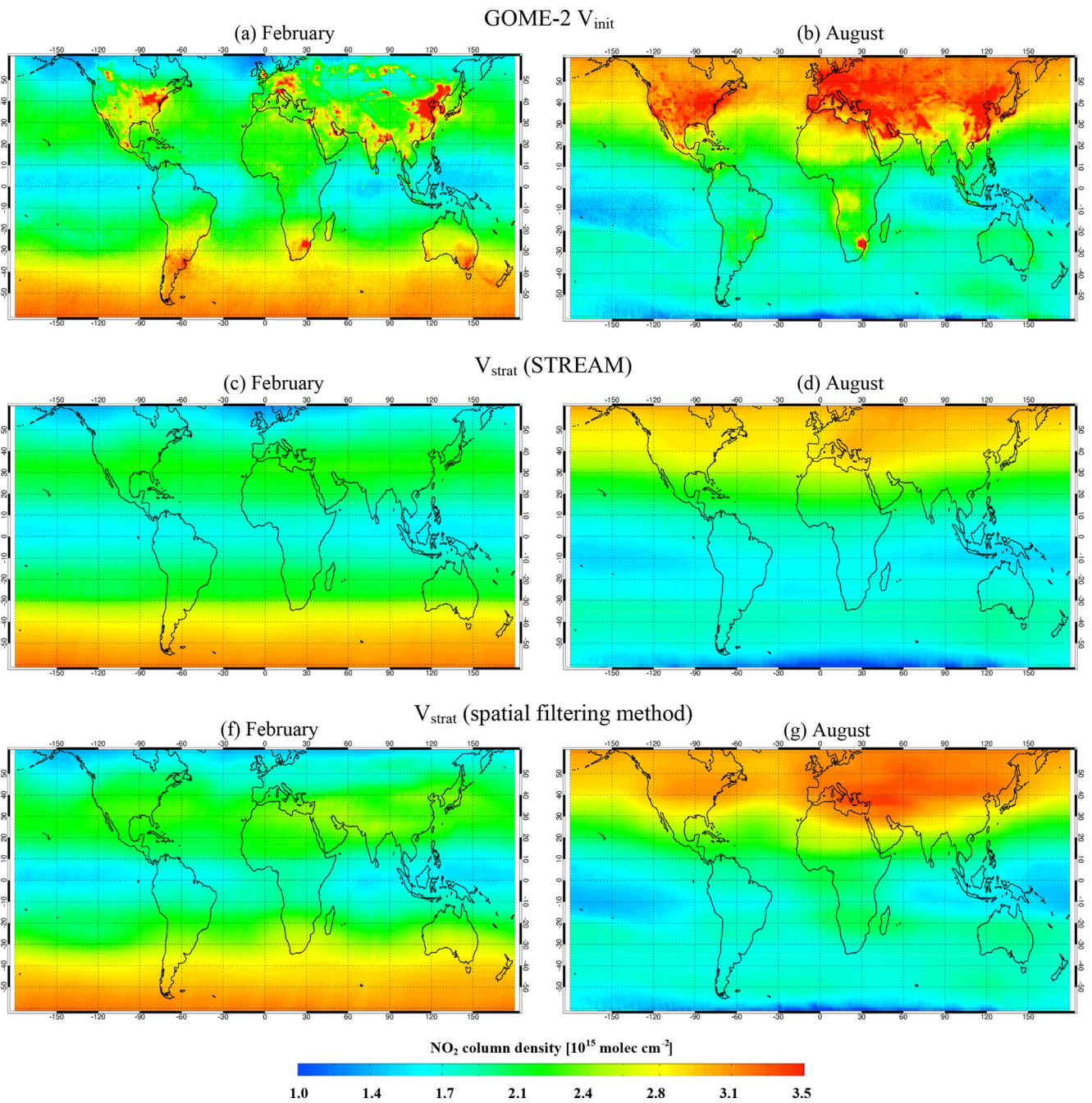


**Figure 9.** GOME-2 initial total NO<sub>2</sub> columns (a, b) and stratospheric NO<sub>2</sub> columns retrieved from the improved STREAM algorithm (c, d) and from the spatial filtering method used in GDP 4.8 (e, f), measured by GOME-2A in February (a, c, e) and August (b, d, f) 2009.

**Table 2.** Main settings of AMF calculation method and input data discussed in this study.

|                  | GDP 4.8   | GDP 4.9 (this work)                         |
|------------------|---|---|
| RTM              | LIDORT v2.2+  | VLIDORT v2.7                                |
| Surface albedo   | TOMS–GOME LER, Boersma et al. (2004)                  | GOME-2 Min-LER v2.1, Tilstra et al. (2017b) |
| A priori profile | Monthly MOZART-2 ( $1.875^\circ \times 1.875^\circ$ ) | Daily TM5-MP ( $1^\circ \times 1^\circ$ )   |

## 6 Improvements to NO<sub>2</sub> AMF calculation

### 6.1 RTM

As summarised in Table 2, updated box-AMFs are calculated using the linearised vector code VLIDORT (Spurr, 2006) version 2.7. VLIDORT applies the discrete ordinates method to generate simulated intensity and analytic intensity derivatives with respect to atmospheric and surface parameters (i.e. weighting functions). Box-AMFs  $m_l$  (see Eq. 3) are determined as

$$m_l = \frac{\partial \ln I}{\partial \tau_{\text{NO}_2,l}} = \frac{\frac{\partial I}{\partial \tau_{\text{NO}_2,l}} \cdot \tau_{\text{NO}_2,l}}{I \cdot \tau_{\text{NO}_2,l}}, \quad (8)$$

with  $I$  being the simulated top-of-atmosphere radiance,  $\tau_{\text{NO}_2,l}$  the absorption optical thickness of NO<sub>2</sub> at layer  $l$ , and term  $\frac{\partial I}{\partial \tau_{\text{NO}_2,l}} \cdot \tau_{\text{NO}_2,l}$  the NO<sub>2</sub> profile weighting function. Compared to the scalar (intensity-only) LIDORT code, VLIDORT provides more realistic modelling results with a treatment of light polarisation, which affects the tropospheric AMFs by up to 4 %.

The box-AMFs  $m_l$  for each layer are calculated for the midpoint wavelength of fitting window, i.e. 461 nm in our NO<sub>2</sub> retrieval, which is representative of the window-averaged box-AMFs. Compared to the tropospheric AMFs at 440 nm (midpoint wavelength in GDP 4.8), the ones calculated at 461 nm are higher by up to 10 % for polluted situations, due to the wavelength dependency of Rayleigh scattering, in agreement with Boersma et al. (2018) (see Fig. 7 therein). Note that the uncertainty related to the wavelength dependency of the AMF is much smaller than the uncertainties introduced by surface albedo, a priori NO<sub>2</sub> profile, cloud, and aerosol (see Sect. 6.4).

The  $m_l$  value is calculated with the RTM and stored in a LUT as a function of GOME-2 viewing geometry, surface pressure, and surface albedo. Compared to the LUT used in the GDP 4.8, a new LUT is calculated with an increased number of reference points, e.g. for surface pressure (from 10 to 16) and for surface albedo (from 10 to 14), as well as vertical layers (from 24 to 60) to reduce the interpolation error (Lorente et al., 2017), leading to differences in tropospheric AMFs by up to 2 %.

### 6.2 Surface albedo

Surface albedo is an important parameter for an accurate retrieval of NO<sub>2</sub> columns and cloud properties. The sensitivity of backscattered radiance to the boundary layer NO<sub>2</sub> is strongly related to the surface albedo, especially over polluted areas. In the GDP 4.9, the surface LER climatology based on TOMS–GOME data (Boersma et al., 2004) has been replaced by one based on GOME-2 observations (Tilstra et al., 2017b). Using the degradation-corrected GOME-2 level 1 measurements, the GOME-2 surface LER is derived by matching the measurements in a

pure Rayleigh scattering atmosphere without clouds. Compared to the TOMS–GOME LER climatology, the GOME-2 surface LER (version 2.1) dataset takes advantage of newer observations for 2007–2013, an increased spatial resolution of 1.0° long. × 1.0° lat. for standard grid cells and 0.25° long. × 0.25° lat. at coastlines (Tilstra et al., 2017a), and an improved treatment of cloud contaminated cells over the ocean.

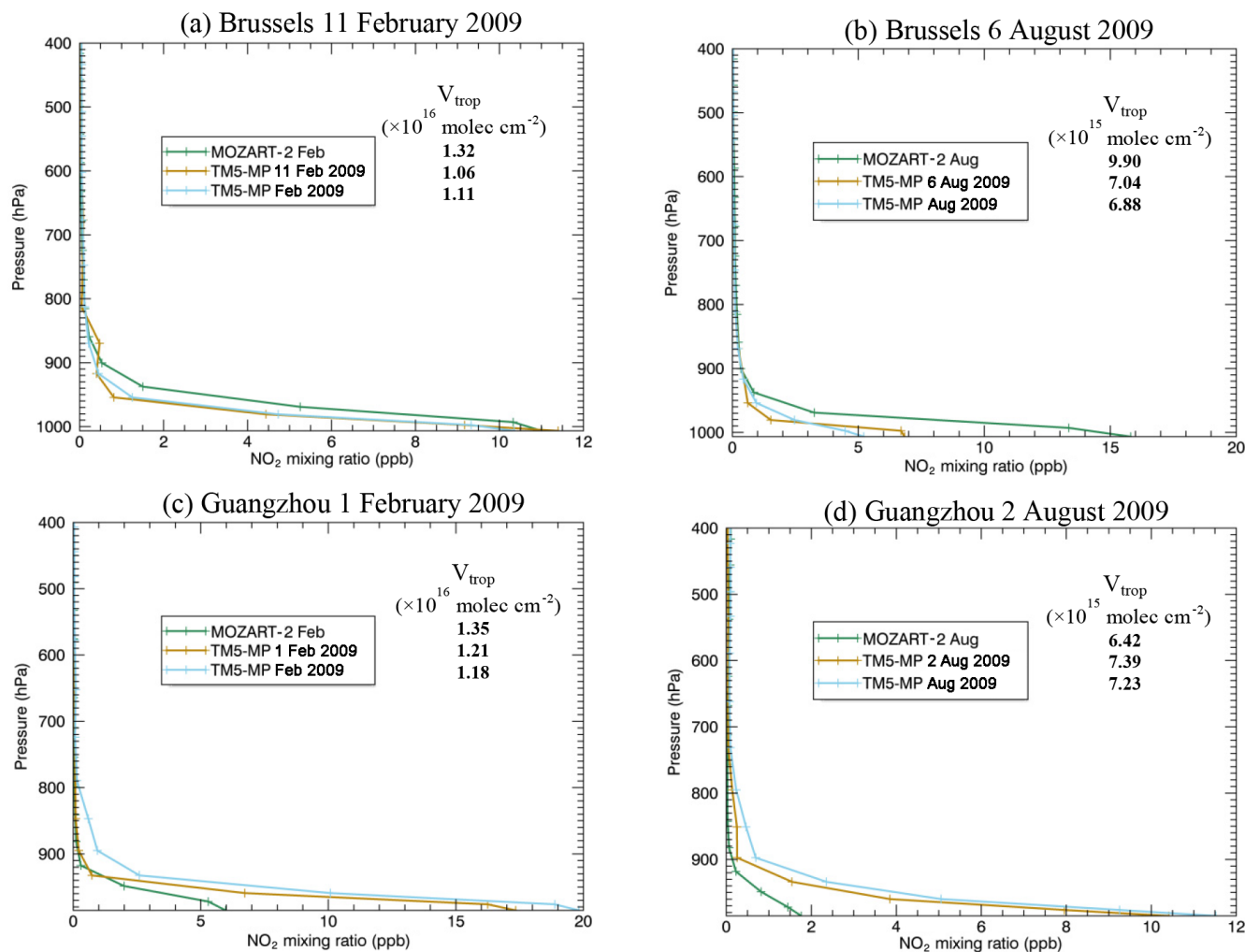
Figure 10 shows the surface LER data from the GOME-2 and TOMS–GOME observations for 440 nm in February. A good overall consistency is found between the two LER datasets, particularly over the ocean. Larger differences are found over certain snow or ice areas, like Russia and southern Canada, which can be attributed to changes in snow or ice cover during the different measurement periods of the two LER datasets. Increased spatial resolution for the GOME-2 LER version 2.1 dataset enables a better representation of surface features for the land–sea boundaries, e.g. coasts around western Europe and eastern China. Improvements in the GOME-2 LER algorithm (Tilstra et al., 2017b) decreases the surface LER values over regions with persistent clouds, e.g. the North Atlantic Ocean and the North Pacific Ocean at middle latitudes. Systematic differences in the LER climatologies are also caused by the different overpass time, observing geometry, and radiometric calibration of the instruments.

Figure 11 illustrates the influence of the updated surface LER at 440 nm on the retrieved tropospheric NO<sub>2</sub> columns in February 2008. The difference over the ocean is very small. Larger effects are noticed primarily under polluted conditions with positive differences, e.g. over parts of central Europe, Russia, or USA, and negative values, e.g. over parts of South Africa, India, or China. The differences in the retrieved tropospheric NO<sub>2</sub> columns are consistent with the changes in the surface LER. For example, the GOME-2 surface LER over central Europe is  $\sim 0.012$  smaller than TOMS–GOME data, and a lower sensitivity to tropospheric NO<sub>2</sub> is therefore assumed in the AMF calculation. This results in a decrease in the AMF and hence an increase in the retrieved tropospheric NO<sub>2</sub> column by  $\sim 7 \times 10^{14}$  molec cm<sup>2</sup> ( $\sim 12$  %). Vice versa, an increase of the surface LER values by  $\sim 0.018$  over the Yangtze River region in eastern China leads to a reduction of tropospheric NO<sub>2</sub> columns by  $\sim 4 \times 10^{15}$  molec cm<sup>2</sup> ( $\sim 15$  %).

As described in Sect. 6.1, the AMFs are calculated for 461 nm in the GDP 4.9 (425–497 nm wavelength window) instead of 440 nm in the GDP 4.8 (with 425–450 nm wavelength window), and therefore the corresponding surface LER values of 463 nm are used. The surface LER values at 463 nm are higher by up to 0.02 over desert areas and lower by up to 0.02 over the ocean and the snow or ice areas, which result in differences of up to 5 % in the calculated AMFs.

The surface LER climatology from Kleipool et al. (2008) derived from OMI measurements for 2004–2007 has been widely used in satellite NO<sub>2</sub> retrievals (e.g. Boersma et al.,



A priori NO<sub>2</sub> profile

**Figure 12.** Examples of a priori NO<sub>2</sub> profiles for Brussels (a, b) and Guangzhou (c, d) on a given day in February (a, c) and August (b, d) 2009. Monthly profiles are shown for MOZART-2 (green), and daily profiles on the given days are shown for TM5-MP (brown) together with the monthly average profiles calculated for TM5-MP (blue). The tropospheric NO<sub>2</sub> columns retrieved using each a priori NO<sub>2</sub> profile are also given.

In Fig. 12, the tropospheric NO<sub>2</sub> columns retrieved for the individual days using TM5-MP and MOZART-2 a priori NO<sub>2</sub> profiles are also reported. Taking Brussels on 11 February 2009 (Fig. 12a) as an example, the smaller boundary layer concentration modelled by TM5-MP (less steep profile shape) leads to an increase in the tropospheric AMF and hence a decrease in the retrieved tropospheric NO<sub>2</sub> columns by  $2.6 \times 10^{15}$  molec cm<sup>2</sup> (19.7%). Figure 13 presents a comparison of the monthly averaged tropospheric NO<sub>2</sub> columns retrieved using daily TM5-MP and monthly MOZART-2 a priori NO<sub>2</sub> profiles in February and August 2009. The application of the daily TM5-MP a priori NO<sub>2</sub> profiles affects the tropospheric NO<sub>2</sub> columns by more than  $1 \times 10^{15}$  molec cm<sup>2</sup> mostly over polluted regions with enhanced NO<sub>2</sub> in the boundary layer, e.g. with an increase of tropospheric NO<sub>2</sub>

over parts of China, India, and South Africa and a decrease over parts of the eastern US, Europe, and Japan.

To analyse the effect of using daily vs. monthly profiles, the tropospheric NO<sub>2</sub> columns are also retrieved using the monthly average TM5-MP profiles, as shown in Fig. 12. Differences in the profile shape of daily and monthly profiles are mainly related to the variations in the meteorology. In agreement with Nüß et al. (2006) and Laughner et al. (2016), the use of monthly profiles changes the tropospheric NO<sub>2</sub> columns by up to  $3 \times 10^{15}$  molec cm<sup>2</sup> depending on the wind speed and wind direction, in particular for regions affected by transport (not shown). For the example of Brussels on 11 February 2009 (Fig. 12a), the use of monthly profiles increases the tropospheric NO<sub>2</sub> columns by  $5 \times 10^{14}$  molec cm<sup>2</sup> (4.7%). A comprehensive analysis of the effect of using a

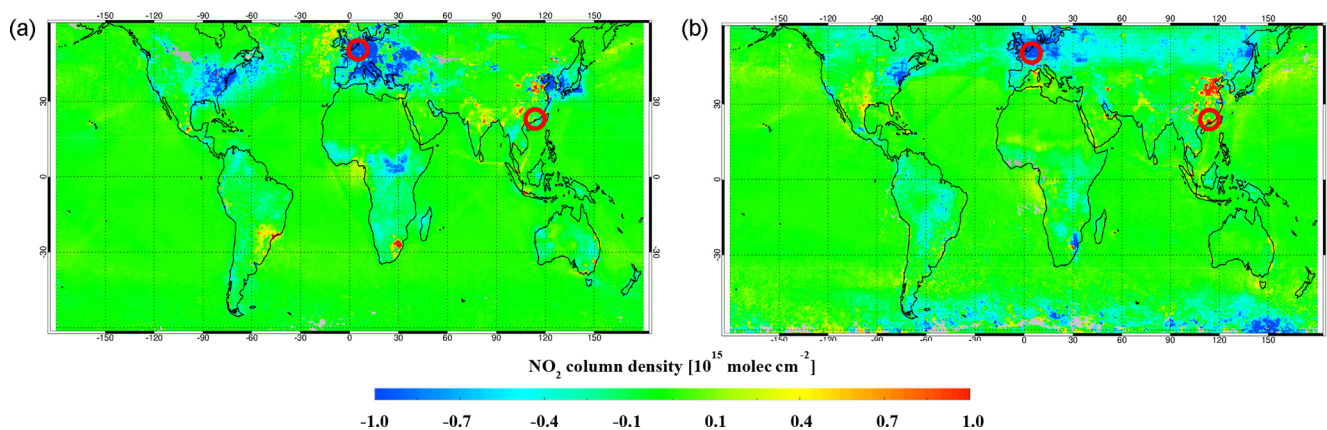


**Figure 13.** Difference in tropospheric NO<sub>2</sub> columns for clear-sky conditions (cloud radiance fraction smaller than 0.5) retrieved using daily TM5-MP and monthly MOZART-2 a priori NO<sub>2</sub> profiles for February (a) and August (b) 2009. Red circles indicate locations in Fig. 12.

priori NO<sub>2</sub> profiles from different chemistry transport models on the retrieved tropospheric NO<sub>2</sub> will be described in a subsequent paper.

#### 6.4 Examples of GOME-2 tropospheric NO<sub>2</sub>

Figure 14 shows the tropospheric NO<sub>2</sub> columns from the improved GDP 4.9 algorithm for February and August averaged for the year 2007–2016. Figure 15 shows the difference in tropospheric NO<sub>2</sub> columns from the GDP 4.9 and GDP 4.8 product. The tropospheric NO<sub>2</sub> columns increase globally by  $\sim 1 \times 10^{14}$  molec cm<sup>2</sup> due to the improved DOAS slant column fitting and increase further by  $\sim 3 \times 10^{14}$  molec cm<sup>2</sup> around moderately polluted regions benefiting from the use of new stratosphere–troposphere separation algorithm STREAM. A stronger change by more than  $1 \times 10^{15}$  molec cm<sup>2</sup> is found mainly over polluted continents as a result of the improvements to the AMF calculation, primarily the surface albedo (which also affects the snow or ice area, e.g. southern Canada and northeastern Europe) and/or the a priori NO<sub>2</sub> profiles (which also affect the polluted ocean, e.g. shipping lanes in southeastern Asia).

Over central northern Europe, the tropospheric NO<sub>2</sub> columns are reduced by  $\sim 1 \times 10^{15}$  molec cm<sup>2</sup> for GDP 4.9 in winter and  $\sim 3 \times 10^{14}$  molec cm<sup>2</sup> in summer. A larger number of negative values in GDP 4.8, possibly related to the overestimated stratospheric NO<sub>2</sub> around polar vortex areas, is largely corrected in GDP 4.9 by improving the stratosphere–troposphere separation algorithm. Over eastern China and eastern US, the seasonal variation is consistent between GDP 4.8 and 4.9, with reduced values in winter (by more than  $1 \times 10^{15}$  molec cm<sup>2</sup>) and enlarged values in summer (by more than  $1 \times 10^{15}$  molec cm<sup>2</sup> for eastern China and  $5 \times 10^{14}$  molec cm<sup>2</sup> for eastern US) for GDP 4.9 due to the combined impact of the algorithm changes, mainly the AMF calculation. Over India and its surrounding areas, a systematic increase in tropospheric NO<sub>2</sub> columns by

$\sim 7 \times 10^{14}$  molec cm<sup>2</sup> for GDP 4.9 benefits from the use of STREAM.

#### 6.5 Uncertainty estimates for GOME-2 total and tropospheric NO<sub>2</sub>

The uncertainty in our GDP 4.9 NO<sub>2</sub> slant columns is  $4.4 \times 10^{14}$  molec cm<sup>2</sup>, calculated from the average slant column error using a statistical method described in Sect. 4.5. The uncertainty in the GOME-2 stratospheric columns is  $\sim 4\text{--}5 \times 10^{14}$  molec cm<sup>2</sup> for polluted conditions based on the daily synthetic GOME-2 data and  $\sim 1\text{--}2 \times 10^{14}$  molec cm<sup>2</sup> for monthly averages. The uncertainty in the GDP 4.9 AMF calculation is likely reduced, considering the improved surface albedo climatology and a priori NO<sub>2</sub> profiles, which are the main causes of AMF structural uncertainty (Lorente et al., 2017). In addition, the AMF uncertainty is substantially driven by the cloud parameters and the aerosol correction approach.

The largest cloud-related uncertainty in NO<sub>2</sub> retrieval is introduced by the surface albedo–cloud fraction error correlation, as analysed by Boersma et al. (2018) for OMI using the OMCLDO<sub>2</sub> cloud product, which requires a surface albedo climatology as input in the cloud fraction retrieval. But this uncertainty is likely smaller for OCRA and ROCINN cloud algorithms, since the surface albedo is treated differently in OCRA’s cloud fraction calculation. Retrieved by separating a spectral scene into cloudy contribution and cloud-free background, the cloud fraction from OCRA is affected by surface albedo through the cloud-free map construction with a larger impact over bright surfaces like snow or ice cover, particularly during snowfall (higher background) or melting (lower background), which has been corrected by interpolating towards a daily value between two monthly cloud-free maps in OCRA (Lutz et al., 2016).

The uncertainty introduced by aerosol in GDP 4.9 is  $\sim 50\%$  for high aerosol loading, in agreement with Lorente

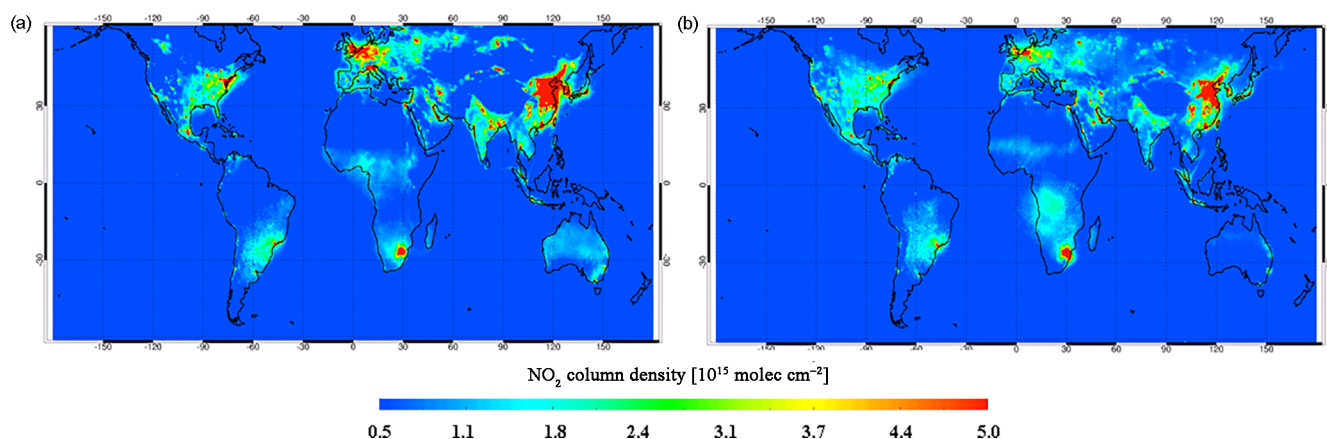


**Figure 14.** Monthly average tropospheric NO<sub>2</sub> columns from GDP 4.9 for clear-sky conditions (cloud radiance fraction smaller than 0.5), measured by GOME-2A in February (a) and August (b) 2007–2016.

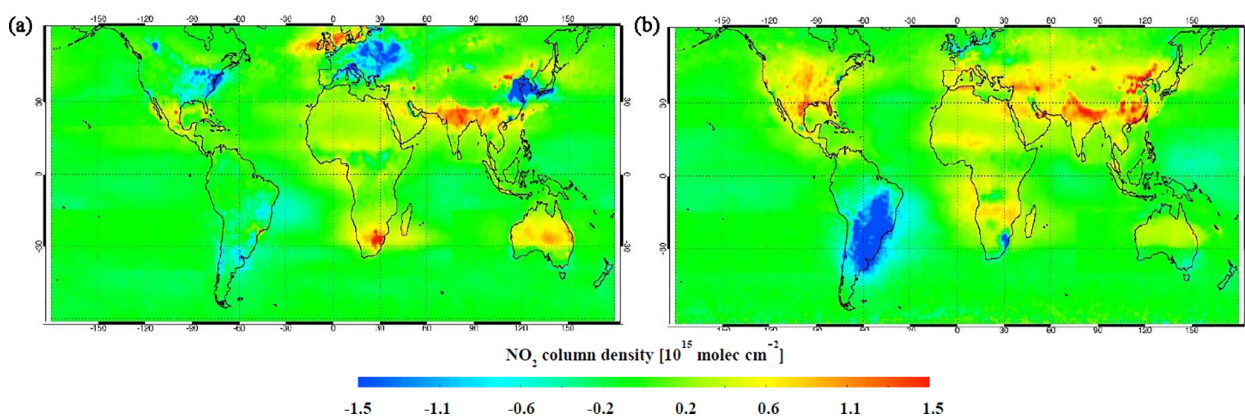


**Figure 15.** Difference in tropospheric NO<sub>2</sub> columns from GDP 4.9 and GDP 4.8 for clear-sky conditions (cloud radiance fraction smaller than 0.5) in February (a) and August (b) 2007–2016 for GOME-2A.

et al. (2017). With direct impact on NO<sub>2</sub> AMF calculation and indirect impact via cloud parameter retrieval, the aerosol effect has been considered for OMI implicitly through the cloud correction (Boersma et al., 2004, 2011) or explicitly with additional aerosol information for regional studies (Lin et al., 2014, 2015; Kuhlmann et al., 2015; Castellanos et al., 2015; Chimot et al., 2018), leading to an increase or decrease of NO<sub>2</sub> AMF by up to 40 % depending on NO<sub>2</sub> distribution and aerosol properties and distribution. Since aerosol is highly variable in space and time due to the dependency on emission sources, transports, and atmospheric processes (Holben et al., 1991), explicit aerosol correction will be applied in our AMF calculation when reliable observations or model outputs of aerosol optical properties and vertical distributions are available. To conclude, the uncertainty in the AMF calculation is estimated to be in the 10 %–45 % range for polluted conditions, leading to a total uncertainty in the tropospheric NO<sub>2</sub> columns likely in the range of 30 %–70 %.

## 7 End-to-end GOME-2 NO<sub>2</sub> validation

The validation of NO<sub>2</sub> data derived from the GOME-2 GDP algorithm is part of the validation activities done at BIRA-IASB in the AC-SAF context (Hassinen et al., 2016). An end-to-end validation approach is usually performed for each main release and summarised in validation reports that can be found on AC-SAF validation website (<http://cdop.aeronomie.be/validation/valid-reports>, last access: 1 February 2019). This includes several steps, such as

1. the DOAS analysis results, cloud property retrievals, and AMF evaluations by confrontation of GOME-2 retrievals to other established satellite retrievals and AMF evaluations;
2. the stratospheric reference evaluation by comparison with correlative observations from ground-based zenith-looking DOAS spectrometers and from other nadir-looking satellites; and

- the tropospheric and total NO<sub>2</sub> column data evaluation by comparison with correlative observations from ground-based MAXDOAS and direct-sun spectrometers (Pinardi et al., 2014).

In this paper, we focus on the last point: the validation of tropospheric data with BIRA-IASB ground-based MAXDOAS data. The MAXDOAS instruments collect scattered sky light in a series of line-of-sight angular directions extending from the horizon to the zenith. High sensitivity towards absorbers near the surface is obtained for the smallest elevation angles, while measurements at higher elevations provide information on the rest of the column. This technique allows the determination of vertically resolved abundances of atmospheric trace species in lowermost troposphere (Hönninger et al., 2004; Wagner et al., 2004; Wittrock et al., 2004; Heckel et al., 2005). Here the bePRO retrieval code (Clémer et al., 2010; Hendrick et al., 2014; Vlemmix et al., 2015) is used to retrieve tropospheric columns and low tropospheric profiles (up to 3.5 km with about 2 to 3 degrees of freedom).

As summarised in Table 3, a set of MAXDOAS stations (Beijing, Bujumbura, Observatoire de Haute-Provence (OHP), Réunion, Uccle, and Xianghe) is providing interesting test cases for GOME-2 sensitivity to tropospheric NO<sub>2</sub>. Indeed Beijing and Uccle are typical urban stations, Xianghe is a suburban station (~ 60 km from Beijing), Bujumbura and Réunion are small cities in remote regions, and OHP is largely rural but occasionally influenced by polluted air masses transported from neighbouring cities. These different station types are important in the validation context as it is generally expected that urban stations are underestimated by the satellite data, due to the averaging of a local source over a pixel size (80 km × 40 km and 40 km × 40 km for GOME-2) larger than the horizontal sensitivity of the ground-based measurements which is about a few to tens of kilometres (Irie et al., 2011; Wagner et al., 2011; Ortega et al., 2015). In this context, MAXDOAS data are already better than in situ measurements with an extended horizontal and vertical sensitivity, more similar to the satellite sensitivity, but differences in sampling and sensitivity still remain and explain part of the biases highlighted by validation exercises. Several validation studies show a significant underestimation of tropospheric trace gases, such as NO<sub>2</sub>, from satellite observations over regions with strong spatial gradients in tropospheric pollution (e.g. Celarier et al., 2008; Kramer et al., 2008; Chen et al., 2009; Irie et al., 2012; Ma et al., 2013; Wu et al., 2013; Kanaya et al., 2014; Wang et al., 2017; Drosoglou et al., 2017, 2018). Other possible explanations include the uncertainties in the applied satellite retrieval assumptions, such as the choices of surface albedo, a priori NO<sub>2</sub> profiles, or cloud and aerosol treatment (Boersma et al., 2004, 2011; Leitão et al., 2010; Heckel et al., 2011; Lin et al., 2014, 2015). The best agreement is generally obtained in the case of suburban and remote stations, but difficulties may arise when small local sources are present in a remote location, such as Réu-

nion island or Bujumbura (Pinardi et al., 2015; Gielen et al., 2017).

The same methodology as in the GDP 4.8 validation report (Pinardi et al., 2015) is used for the validation of this improved GDP 4.9 tropospheric NO<sub>2</sub> dataset; the satellite data are filtered for clouds (cloud radiance fraction smaller than 0.5), and the mean value of all the valid pixels within 50 km of the stations is compared to the ground-based value. The original ground-based MAXDOAS data usually retrieve NO<sub>2</sub> columns all day long every 20 to 30 min, and these values are linearly interpolated to the GOME-2 overpass time (09:30 LT) if original data exist within ±1 h.

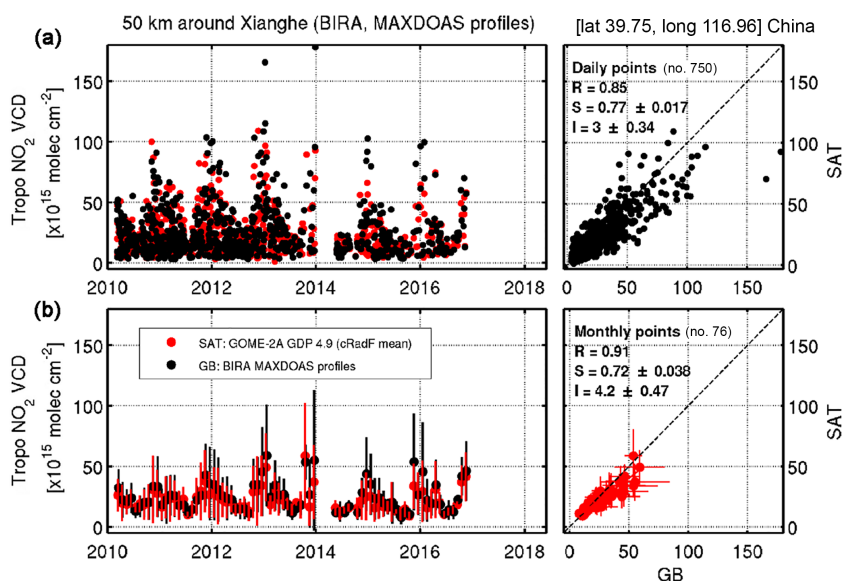
Figure 16 shows an example of the time series and scatter plot of the daily and monthly mean comparison between GDP 4.9 tropospheric NO<sub>2</sub> columns and ground-based MAXDOAS measurements in Xianghe, including the statistical information on the number of points, correlation coefficient, slope, and intercept of orthogonal regression analysis. Figure 17 presents the daily and monthly mean absolute and relative differences of GDP 4.9 and ground-based measurements. As can be seen in Figs. 16 and 17, the seasonal variation in the tropospheric NO<sub>2</sub> columns is similarly captured by both observation systems, with differences on average within  $\pm 3 \times 10^{15}$  molec cm<sup>2</sup> (median difference of  $-1.2 \times 10^{15}$  molec cm<sup>2</sup>). Larger differences are observed on some days and months, particularly in winter when NO<sub>2</sub> and aerosol loadings are large. A relatively compact scatter is found, with a correlation coefficient of 0.91 and a slope of  $0.72 \pm 0.04$  for the orthogonal regression fit. These results are qualitatively similar to those obtained in previous validation exercises (Celarier et al., 2008; Kramer et al., 2008; Chen et al., 2009; Irie et al., 2012; Ma et al., 2013; Wu et al., 2013; Kanaya et al., 2014; Wang et al., 2017; Drosoglou et al., 2017, 2018). Similar figures for GDP 4.8 can be found on the AC-SAF validation website (<http://cdop.aeronomie.be/validation/valid-results>, last access: 1 February 2019).

Figure 18 reports the monthly mean absolute and relative differences for both GDP 4.8 and GDP 4.9 for Xianghe station. The daily differences are also reported through the histogram panel, where the reduction in the spread of the daily comparison points is clearly visible for GDP 4.9. The reduction of the bias, which is smaller and more stable in time, is seen in the absolute and relative monthly mean bias time series. A total of 3 years show a standard deviation of the monthly biases larger for GDP 4.9 than for GDP 4.8 ( $\pm 12\%$  instead of  $\pm 8\%$  in 2010,  $\pm 12\%$  instead of  $\pm 8\%$  in 2013, and  $\pm 41\%$  instead of  $\pm 27\%$  in 2014) but with a strongly reduced mean bias ( $-4\%$  instead of  $-20\%$ ,  $-8\%$  instead of  $-34\%$ , and  $-1\%$  instead of  $-44\%$ ).

Similar figures as Figs. 16 and 18 for all the stations are gathered in Figs. S1 to S4 in the Supplement, and all the statistics are summarised in Tables 4 and 5 for GOME-2A and GOME-2B, respectively. Figures S1 and S2 in the Supplement present the time series and scatter plots for GDP 4.9, while Figs. S3 and S4 in the Supplement present the differ-

**Table 3.** An overview of BIRA-IASB MAXDOAS datasets used in this study.

| MAXDOAS station | Period          | Position                 | Description                                    |
|-----------------|-----------------|--------------------------|--|
| Beijing         | 6/2008–4/2009   | Lat. 39.98, long. 116.38 | urban polluted site in China                   |
| Bujumbura       | 12/2013–11/2016 | Lat. −3.38, long. 29.38  | urban site in Burundi                          |
| OHP             | 3/2007–11/2016  | Lat. 43.94, long. 5.71   | background site in southern France             |
| Réunion         | 4/2016–11/2016  | Lat. −21, long. 55.3     | urban site in Réunion island                   |
| Uccle           | 4/2011–11/2016  | Lat. 51, long. 4.36      | urban polluted site in Belgium with a miniDOAS |
| Xianghe         | 3/2010–11/2016  | Lat. 39.75, long. 116.96 | suburban polluted site in China                |

**Figure 16.** Daily (a) and monthly mean (b) time series and scatter plots of GOME-2A and MAXDOAS tropospheric NO<sub>2</sub> columns (mean value of all the pixels within 50 km around Xianghe).

ences for both GDP 4.9 and GDP 4.8 comparisons. As discussed in Pinardi et al. (2015), for background stations (here Bujumbura, Réunion, and OHP), the mean bias is considered the best indicator of the validation results, due to the relatively small variability in the measured NO<sub>2</sub>. In urban (Beijing and Uccle) and suburban (Xianghe) situations, the NO<sub>2</sub> variability is large enough and in this case, the correlation coefficient is a good indication of the linearity or coherence of the satellite and ground-based dataset, although a larger difference in terms of slope (closer to 0.5 than to 1 for urban cases) and mean bias can be expected because satellite measurements (and especially GOME-2 80 km × 40 km and 40 km × 40 km pixels) smooth out the local NO<sub>2</sub> hot spots. This can be seen, e.g. in the cases of Beijing and Xianghe for GOME-2A (see Fig. S1a in the Supplement and Fig. 16, respectively), where very high correlations ( $R = 0.94$  and  $0.91$ , respectively) are obtained from GDP 4.9, showing the very consistent behaviour of both datasets for small and large NO<sub>2</sub> columns, while their slopes ( $S = 0.4$  and  $0.72$ , respectively) show almost a factor of 2 difference, with a smaller slope in the Beijing case, where the MAXDOAS instrument is in the city centre and thus much more subject to local emis-

sion smeared out by the GOME-2 large pixel. This last effect is also seen through the bias values ( $RD = -47\%$  and  $-5.8\%$ , respectively) that are strongly reduced when moving the MAXDOAS outside the city in a suburban location like Xianghe. A slope of 0.47 (similar to the 0.4 of Beijing) is also obtained in Uccle, another urban site, where the MAXDOAS is affected by local emissions.

In remote cases such as OHP, Bujumbura, or Réunion island, as discussed above, the variation of the NO<sub>2</sub> columns is small and the statistical analysis on the regression is not very representative of the situation, with a cloud of points giving small slopes and low correlation coefficients (see e.g. Fig. S1b–d in the Supplement and Table 4 for GOME-2A). In those cases, GOME-2 is lower than the ground-based measurements, with sometimes almost no seasonal variation, e.g. Bujumbura and Réunion, and in other cases, like OHP, some of the daily peaks are captured by GOME-2 (as days in the winter of 2014 and 2015), and the seasonal patterns and the orders of magnitude of both datasets are similar. In these cases, it is best to look at the absolute biases (as relative biases are large due to the division with small ground-based columns), as presented in e.g. Fig. S3b–d and Table 4.

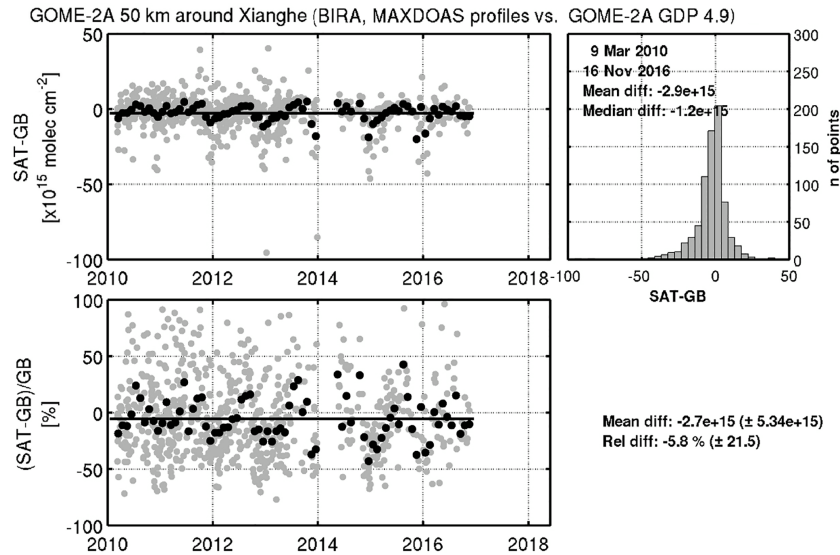


**Figure 17.** Daily (grey dots) and monthly mean (back dots) absolute and relative GOME-2A and MAXDOAS time series differences for the Xianghe station. The histogram of the daily differences is also given, with the mean and median difference, and the total time-series absolute and relative monthly differences are given outside the panels.

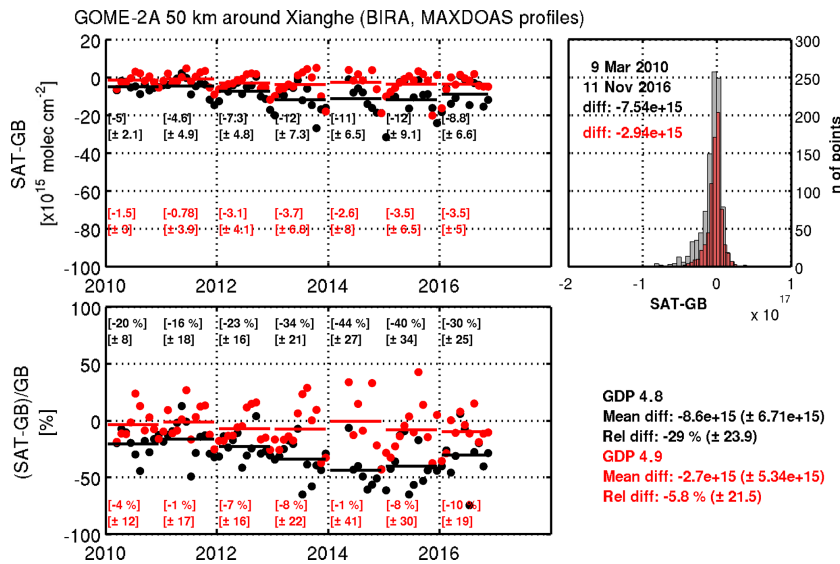


**Figure 18.** Absolute and relative differences of GOME-2A and MAXDOAS tropospheric NO<sub>2</sub> columns. The time series presents the monthly mean differences for GDP 4.8 (black) and GDP 4.9 (red). The total mean difference values and standard deviations are given, as well as the yearly values. The histogram presents the daily differences over the whole time series for the two products (grey for GDP 4.8 and red for GDP 4.9).

Mean absolute differences for GDP 4.9 are about  $-3.6 \times 10^{15}$  molec cm<sup>2</sup> for Bujumbura,  $-8.5 \times 10^{14}$  molec cm<sup>2</sup> for OHP, and  $-1.5 \times 10^{15}$  molec cm<sup>2</sup> for Réunion, which are all smaller than their respective GDP 4.8 values. The daily differences presented in the histograms of those figures also show reduced spread of GDP 4.9 comparisons when superposed to the GDP 4.8 results. Similar differences are also found for GOME-2B.

To conclude, although the Xianghe case presented in Figs. 16 to 18 is the best case (due to its suburban location and its long time series), better seasonal agreement between GDP 4.9 and MAXDOAS data is found for urban and suburban cases like Beijing, Uccle, and Xianghe, compared to results with GDP 4.8. In remote locations such as OHP, which is occasionally influenced by polluted air masses transported from neighbouring cities, the comparison is also meaningful (e.g. with a mean bias reduced from  $-45\%$  for GDP 4.8

to  $-25\%$  for GDP 4.9 for GOME-2A), while cases such as Bujumbura and Réunion are quite challenging for satellite validation, with specific local conditions (Bujumbura is in a valley on the side of Lake Tanganyika, while the MAXDOAS at Réunion is in St-Denis, on the coast of the 65 km long and 50 km wide island in the Indian Ocean, containing a mountain massif with summits above 2740 m a.s.l.). In both cases the MAXDOAS instrument is located in small cities surrounded by specific orography, difficult for satellite retrievals and challenging for validation. The absolute and relative differences show, however, a clear improvement for all the stations when comparing to GDP 4.8 results for both daily and monthly mean biases. The daily biases and spreads are all reduced.

To summarise, the impact of the improvement of the algorithm (as seen in Tables 4 and 5 and in Figs. S3 and S4 in the Supplement) leads to a decrease of the relative differences in urban conditions such as in Beijing or Uccle from  $[-52, -60]\%$  for GDP 4.8 to  $[-43, -47]\%$  for GDP 4.9 for GOME-2A and from  $-54\%$  to  $-40\%$  for GOME-2B. In suburban conditions such as in Xianghe, the differences go from  $-30\%$  to  $-6\%$  for GOME-2A and from  $-26\%$  to  $-2\%$  for GOME-2B. In remote (difficult) cases such as in Bujumbura or Réunion, the differences go from  $[-89, -90]\%$  to  $[-64, -76]\%$  for GOME-2A and from  $[-86, -87]\%$  to  $[-47, -74]\%$  for GOME-2B, while in background cases such as in OHP, the differences decrease from  $-45\%$  to  $-25\%$  for GOME-2A and from  $-42\%$  to  $-17\%$  for GOME-2B. The differences in numbers for GOME-2A and GOME-2B are due to the different time-series lengths of both comparisons (e.g. March 2010–November 2016 for GOME-2A and December 2012–November 2016 for GOME-2B in Xianghe), the different sampling of the atmosphere by GOME-2A and GOME-2B (slight time delay between both overpasses and reduced swath pixels for GOME-2A since July 2013), and the impact of the decreasing quality of the satellite in time, i.e. the GOME-2A degradation (Dikty et al., 2011; Munro et al., 2016). This lead, e.g. for Xianghe, to  $-2\%$  bias and 0.49 slope for GOME-2B compared to  $-6\%$  and 0.72 for GOME-2A for GDP 4.9.

These comparisons results aim at showing how the final GDP 4.9 product is improved compared to its predecessor, and not to summarise the improvements of each of the changes discussed in previous sections. In addition, the specific validation method could be improved or at least better characterised (including results uncertainties), by, e.g. changing the colocation method (averaging the MAXDOAS within 1 h of the satellite overpass or selecting the closest satellite pixel, or only considering the pixels containing the station, etc.), but this is out of the scope of the present paper that wants to compare to standard validation results performed routinely on GDP 4.8 (and publicly available at <http://cdop.aeronomie.be/validation/valid-results>, last access: 1 February 2019).

For most stations, in addition of the tropospheric columns, MAXDOAS retrieved NO<sub>2</sub> profiles can also be exploited with satellite column averaging kernels (AKs) to further investigate the impact of the satellite a priori NO<sub>2</sub> profiles in the comparison differences (Eskes and Boersma, 2003). The satellite AK describes the vertical sensitivity of measurements to NO<sub>2</sub> concentrations and relates the MAXDOAS profiles to satellite column measurements by calculating the “smoothed MAXDOAS columns” as

$$V_{\text{MAXDOAS,smoothed}} = \sum_l \text{AK}_{\text{sat},l} \times x_{\text{MAXDOAS},l} \quad (9)$$

The smoothed MAXDOAS NO<sub>2</sub> columns  $V_{\text{MAXDOAS,smoothed}}$  are derived for each day by convolving the layer ( $l$ )-dependent daily profile (interpolated to the satellite overpass time)  $x_{\text{MAXDOAS}}$  expressed in partial columns with the satellite column averaging kernel  $\text{AK}_{\text{sat}}$ .

The comparisons of satellite and smoothed MAXDOAS columns for the different stations are reported in the supplement (Figs. S5 and S6 in the Supplement) and Tables 4 and 5. The different impact of MAXDOAS smoothing on the 2 GDP products results from the different AKs as parameters like surface albedo or a priori NO<sub>2</sub> profiles used in both satellite retrievals are quite different (see Sect. 6). In general, the use of smoothing reduces the MAXDOAS columns and thus reduces both the daily and monthly differences of satellite and MAXDOAS columns. When the average kernels are used to remove the contribution of a priori NO<sub>2</sub> profile shape, as seen in Tables 4 and 5 and in Figs. S5 and S6 in the Supplement, the relative differences in urban conditions such as in Beijing or Uccle decrease from  $[-52, -57]\%$  for GDP 4.8 to  $[-34, -37]\%$  for GDP 4.9 for GOME-2A and from  $-56\%$  to  $-29\%$  for GOME-2B. The differences go from  $-32\%$  to  $-13\%$  for GOME-2A and from  $-27\%$  to  $-11\%$  for GOME-2B for suburban conditions such as in Xianghe and go from  $-77\%$  to  $-31\%$  for GOME-2A and from  $-64\%$  to  $-7\%$  for GOME-2B for remote conditions such as in Réunion.

The results obtained here are coherent with other validation exercises at different stations and with other satellite products, where the NO<sub>2</sub> levels are underestimated by the satellite sensors, e.g. with differences of 5% to 25% over China (Ma et al., 2013; Wu et al., 2013; Wang et al., 2017; Drosoglou et al., 2018), mostly explained by the relatively low sensitivity of space-borne measurements near the surface, the gradient-smoothing effect, and the aerosol shielding effect. These effects are often inherent to the different measurements types or the specific conditions of the validation sites (as seen for the different results for Beijing and Xianghe sites in this paper), but also to the remaining impact of structural uncertainties (Boersma et al., 2016), such as the impact of the choices of the a priori NO<sub>2</sub> profiles and/or the albedo database assumed for the satellite AMF calculations (see Sect. 6). Lorente et al. (2017) estimated, e.g. the AMF structural uncertainty to be on average 42% over polluted

**Table 4.** Averaged absolute differences (AD, SAT-GB in  $10^{15}$  molec cm<sup>2</sup>), relative differences (RD, (SAT-GB)/GB in %), standard deviation (SD), correlation coefficient  $R$ , and regression parameters (slope  $S$  and intercept  $I$ ) of the orthogonal regression for the monthly means GOME-2A tropospheric NO<sub>2</sub> product when comparing to MAXDOAS data. Values for GDP 4.9 (this study) are given and the values for GDP 4.8 are reported in brackets for comparison. Results for both the original comparisons and the smoothed comparisons (smo.) are reported.

|                  | AD $\pm$ SD ( $\times 10^{15}$ ); RD (%)               | $R$         | Regression parameters   |
|------------------|--|-------------|---|
| Beijing          | $-16 \pm 7.3$ ; $-47\%$ ( $-21 \pm 4.5$ ; $-60\%$ )    | 0.94 (0.95) | $S = 0.4 \pm 0.05$ , $I = 3.4 \pm 0.6$ ( $S = 0.58 \pm 0.06$ , $I = -6.2 \pm 0.7$ )     |
| Beijing (smo.)   | $-11 \pm 6.5$ ; $-37\%$ ( $-16 \pm 6.3$ ; $-52\%$ )    | 0.94 (0.96) | $S = 0.43 \pm 0.05$ , $I = 4.4 \pm 0.6$ ( $S = 0.48 \pm 0.04$ , $I = 0.11 \pm 0.5$ )    |
| Bujumbura        | $-3.6 \pm 1.8$ ; $-76\%$ ( $-3.7 \pm 1.1$ ; $-89\%$ )  | n/a (0.29)  | n/a ( $S = 0.1 \pm 0.05$ , $I = 0.012 \pm 0.12$ )                                       |
| Bujumbura (smo.) | $-1.9 \pm 1.2$ ; $-62\%$ ( $-2.4 \pm 0.8$ ; $-84\%$ )  | n/a (0.51)  | n/a ( $S = 0.22 \pm 0.06$ , $I = -0.18 \pm 0.1$ )                                       |
| OHP              | $-0.85 \pm 1$ ; $-25\%$ ( $-1.2 \pm 0.7$ ; $-45\%$ )   | 0.4(0.69)   | $S = 0.25 \pm 0.06$ , $I = 1.2 \pm 0.1$ ( $S = 0.73 \pm 0.07$ , $I = -0.5 \pm 0.1$ )    |
| Réunion          | $-1.5 \pm 0.5$ ; $-64\%$ ( $-1.9 \pm 0.4$ ; $-90\%$ )  | 0.14 (0.23) | $S = 0.05 \pm 0.12$ , $I = 0.64 \pm 0.2$ ( $S = 0.06 \pm 0.06$ , $I = 0.12 \pm 0.08$ )  |
| Réunion (smo.)   | $-0.4 \pm 0.4$ ; $-31\%$ ( $-0.7 \pm 0.2$ ; $-77\%$ )  | 0.15 (0.28) | $S = 0.12 \pm 0.25$ , $I = 0.06 \pm 0.09$ ( $S = 0.32 \pm 0.25$ , $I = -0.01 \pm 0.2$ ) |
| Uccle            | $-5 \pm 2.7$ ; $-43\%$ ( $-6.2 \pm 3.7$ ; $-52\%$ )    | 0.82 (0.49) | $S = 0.47 \pm 0.04$ , $I = 0.83 \pm 0.2$ ( $S = 0.35 \pm 0.08$ , $I = 1.1 \pm 0.4$ )    |
| Uccle (smo.)     | $-3.8 \pm 2.8$ ; $-34\%$ ( $-7.6 \pm 4.3$ ; $-57\%$ )  | 0.75 (0.51) | $S = 0.45 \pm 0.05$ , $I = 0.15 \pm 0.05$ ( $S = 0.28 \pm 0.06$ , $I = 1.5 \pm 0.3$ )   |
| Xianghe          | $-2.7 \pm 5.3$ ; $-5.8\%$ ( $-9.2 \pm 7.1$ ; $-30\%$ ) | 0.91 (0.86) | $S = 0.72 \pm 0.04$ , $I = 4.2 \pm 0.5$ ( $S = 0.63 \pm 0.04$ , $I = 1.3 \pm 0.5$ )     |
| Xianghe (smo.)   | $-6.1 \pm 8.8$ ; $-13\%$ ( $-11 \pm 9.6$ ; $-32\%$ )   | 0.92 (0.9)  | $S = 0.52 \pm 0.03$ , $I = 7.4 \pm 0.4$ ( $S = 0.48 \pm 0.03$ , $I = 4.3 \pm 0.5$ )     |

n/a denotes values that are not applicable.

**Table 5.** Same as Table 4 but for GOME-2B product.

|                  | AD $\pm$ SD ( $\times 10^{15}$ ); RD (%)              | $R$         | Regression parameters   |
|------------------|---|-------------|---|
| Bujumbura        | $-2.8 \pm 0.9$ ; $-74\%$ ( $-3.4 \pm 1$ ; $-87\%$ )   | 0.14 (0.09) | $S = 0.05 \pm 0.06$ , $I = 0.76 \pm 0.12$ ( $S = 0.03 \pm 0.06$ , $I = 0.34 \pm 0.1$ )  |
| Bujumbura (smo.) | $-1.3 \pm 0.7$ ; $-57\%$ ( $-2 \pm 0.8$ ; $-81\%$ )   | 0.28 (0.35) | $S = 0.14 \pm 0.06$ , $I = 0.06 \pm 0.04$ ( $S = 0.15 \pm 0.06$ , $I = 0.08 \pm 0.1$ )  |
| OHP              | $-0.5 \pm 0.7$ ; $-17\%$ ( $-1 \pm 0.6$ ; $-42\%$ )   | 0.13 (0.52) | $S = 0.11 \pm 0.13$ , $I = 1.5 \pm 0.2$ ( $S = 0.82 \pm 0.2$ , $I = -0.6 \pm 0.3$ )     |
| Réunion          | $-0.8 \pm 0.3$ ; $-47\%$ ( $-1.6 \pm 0.3$ ; $-86\%$ ) | 0.56 (0.26) | $S = 0.71 \pm 0.4$ , $I = -0.36 \pm 0.52$ ( $S = 0.08 \pm 0.06$ , $I = 0.13 \pm 0.09$ ) |
| Réunion (smo.)   | $0.05 \pm 0.2$ ; $6.7\%$ ( $-0.5 \pm 0.2$ ; $-64\%$ ) | 0.78 (0.14) | $S = -2.5 \pm 0.8$ , $I = -0.12 \pm 0.22$ ( $S = 0.38 \pm 0.6$ , $I = 0.004 \pm 0.5$ )  |
| Uccle            | $-4.2 \pm 2.4$ ; $-40\%$ ( $-5.6 \pm 3.1$ ; $-54\%$ ) | 0.71 (0.71) | $S = 0.53 \pm 0.09$ , $I = 0.47 \pm 0.4$ ( $S = 0.64 \pm 0.1$ , $I = -1.7 \pm 0.5$ )    |
| Uccle (smo.)     | $-2.8 \pm 2.5$ ; $-29\%$ ( $-6.8 \pm 3.4$ ; $-56\%$ ) | 0.69 (0.73) | $S = 0.53 \pm 0.09$ , $I = 0.13 \pm 0.09$ ( $S = 0.52 \pm 0.11$ , $I = -1 \pm 0.4$ )    |
| Xianghe          | $-3 \pm 9.4$ ; $-2.2\%$ ( $-8.4 \pm 8.7$ ; $-26\%$ )  | 0.87 (0.84) | $S = 0.49 \pm 0.04$ , $I = 9.6 \pm 0.66$ ( $S = 0.6 \pm 0.05$ , $I = 2.5 \pm 0.7$ )     |
| Xianghe (smo.)   | $-6.4 \pm 13$ ; $-11\%$ ( $-11 \pm 12$ ; $-27\%$ )    | 0.89 (0.89) | $S = 0.38 \pm 0.03$ , $I = 11 \pm 0.6$ ( $S = 0.46 \pm 0.03$ , $I = 5.2 \pm 0.58$ )     |

regions and 31 % over unpolluted regions, mostly driven by substantial differences in the a priori trace gas profiles, surface albedo and cloud parameters used to represent the state of the atmosphere. However, the differences in Bujumbura are still of  $-62\%$ , because of the peculiar condition with the MAXDOAS being in a valley, close to Lake Tanganyika, which always leads to a higher surface pressure for the satellite pixels due to the information coming from the a priori model. This is leading to large representation errors and uncertainties in the comparisons (Boersma et al., 2016) that needs to be investigated in more details.

## 8 Conclusions

NO<sub>2</sub> columns retrieved from measurements of the GOME-2 aboard the MetOp-A and MetOp-B platforms have been successfully applied in many studies. The abundance of NO<sub>2</sub> is retrieved from the narrow band absorption structures of NO<sub>2</sub> in the backscattered and reflected radiation in the visible spectral region. The current operational retrieval algorithm (GDP 4.8) for total and tropospheric NO<sub>2</sub> from GOME-2 was first introduced by Valks et al. (2011), and an improved algorithm (GDP 4.9) is described in this paper.

To calculate the NO<sub>2</sub> slant columns, a larger 425–497 nm wavelength fitting window is used in the DOAS fit to increase the signal-to-noise ratio. Absorption cross sections are updated and a linear intensity offset correction is applied. The long-term and in-orbit variations of GOME-2 slit function are corrected by deriving effective slit functions with a stretched preflight GOME-2 slit function and by including a resolution correction function as a pseudo absorber cross section in the DOAS fit, respectively. Compared to the GDP 4.8 algorithm, the NO<sub>2</sub> columns from GDP 4.9 are higher by  $\sim 1\text{--}3 \times 10^{14}$  molec cm<sup>2</sup> (up to 27 %) and the NO<sub>2</sub> slant column noise is lower by  $\sim 24\%$ . In addition, the effect of using a new version (6.1) of the GOME-2 level 1b data has been analysed in our NO<sub>2</sub> algorithm. The application of new GOME-2 level 1b data largely reduces the offset between GOME-2A and GOME-2B NO<sub>2</sub> columns by removing calibration artefacts in the GOME-2B irradiances (due to Xe-line contaminations in the calibration key data). Compared to the GOME-2 NO<sub>2</sub> product from the QA4ECV project, the NO<sub>2</sub> columns from GDP 4.9 show good consistency and the NO<sub>2</sub> slant column noise is  $\sim 14\text{--}28\%$  smaller, indicating a good overall quality of the improved DOAS retrieval.

The stratosphere–troposphere separation algorithm STREAM, which was designed for TROPOMI, was optimised for GOME-2 instrument. Compared to the spatial filtering method used in the GDP 4.8, STREAM provides an improved treatment of polluted and cloudy pixels by defining weighting factors for each measurement depending on polluted situation and cloudy information. For the adaption to GOME-2 measurements, the performance of STREAM is analysed by applying it to synthetic GOME-2 data and by comparing the difference between estimated and original stratospheric fields. Applied to synthetic GOME-2 data calculated by a RTM using C-IFS model data, the estimated stratospheric NO<sub>2</sub> columns from STREAM show good consistency with the a priori truth. A slight overestimation by  $\sim 1\text{--}2 \times 10^{14}$  molec cm<sup>2</sup> is found over lower latitudes, and larger differences of up to  $\sim 5 \times 10^{14}$  molec cm<sup>2</sup> are found at higher latitudes. To reduce the biases over the subtropical regions in winter, an improved latitudinal correction is used in STREAM. Applied to GOME-2 measurements, the updated STREAM successfully separates the stratospheric and tropospheric contribution over polluted regions, especially in the Northern Hemisphere. Compared to the current method in the GDP 4.8, the use of STREAM slightly decreases the stratospheric NO<sub>2</sub> columns by  $\sim 1 \times 10^{14}$  molec cm<sup>2</sup> in general and largely reduces the overestimation over polluted areas.

To improve the calculation of NO<sub>2</sub> AMF, a new box-AMF LUT was generated using the latest version of the VLIDORT RTM with an increased number of reference points and vertical layers to reduce interpolation errors. The new GOME-2 surface LER climatology (Tilstra et al., 2017b) used in this study is derived with a high resolution of  $1^\circ$  long.  $\times 1^\circ$  lat. ( $0.25^\circ$  long.  $\times 0.25^\circ$  lat. at coastlines) and an improved LER algorithm based on observations for 2007–2013. Daily a priori NO<sub>2</sub> profiles, obtained from the chemistry transport model TM5-MP, capture the short-term variability in the NO<sub>2</sub> fields with a resolution of  $1^\circ$  long.  $\times 1^\circ$  lat. A large impact on the retrieved tropospheric NO<sub>2</sub> columns (more than 10 %) is found over polluted areas.

The uncertainty in our GDP 4.9 NO<sub>2</sub> slant columns is  $4.4 \times 10^{14}$  molec cm<sup>2</sup>, calculated from the average slant column error using a statistical method described in Sect. 4.5. The uncertainty in the GOME-2 stratospheric columns is  $\sim 4\text{--}5 \times 10^{14}$  molec cm<sup>2</sup> for polluted conditions based on the daily synthetic GOME-2 data and  $\sim 1\text{--}2 \times 10^{14}$  molec cm<sup>2</sup> for monthly averages. The uncertainty in the tropospheric AMFs is estimated to be in the 10 %–45 % range, considering the use of updated box-AMF LUT and improved surface albedo climatology and a priori NO<sub>2</sub> profiles, resulting in a total uncertainty in the tropospheric NO<sub>2</sub> columns likely in the range of 30 %–70 % for polluted conditions.

An end-to-end validation of the improved GOME-2 GDP 4.9 dataset was performed by comparing the GOME-2 tropospheric NO<sub>2</sub> columns with BIRA-IASB ground-based MAXDOAS measurements. The validation was illustrated

for different MAXDOAS stations (Beijing, Bujumbura, OHP, Réunion, Uccle, and Xianghe) covering urban, suburban, and background situations. Taking Xianghe station as an example, the GDP 4.9 dataset shows a similar seasonal variation in the tropospheric NO<sub>2</sub> columns as the MAXDOAS measurements with a relative difference of  $-5.8\%$  (i.e.  $-2.7 \times 10^{15}$  molec cm<sup>2</sup> in absolute) and a correlation coefficient of 0.91 for GOME-2A, indicating good agreement. The Xianghe site, by its suburban nature, is the best site for validation. At the other sites, mean biases range from ( $-47\%$ ;  $-16 \times 10^{15}$  molec cm<sup>2</sup>) for Beijing, ( $-76\%$ ,  $-74\%$ ;  $-3.6 \times 10^{15}$  molec cm<sup>2</sup>,  $-2.8 \times 10^{15}$  molec cm<sup>2</sup>) for Bujumbura, ( $-25\%$ ,  $-17\%$ ;  $-0.9 \times 10^{15}$  molec cm<sup>2</sup>,  $-0.5 \times 10^{15}$  molec cm<sup>2</sup>) for OHP, ( $-64\%$ ,  $-47\%$ ;  $-1.5 \times 10^{15}$  molec cm<sup>2</sup>,  $-0.8 \times 10^{15}$  molec cm<sup>2</sup>) for Réunion, and ( $-43\%$ ,  $-40\%$ ;  $-5 \times 10^{15}$  molec cm<sup>2</sup>,  $-4.2 \times 10^{15}$  molec cm<sup>2</sup>) for Uccle. Réunion and Bujumbura are difficult sites for validation, due to their valley and mountain nature, while urban sites Beijing and Uccle show similar relative results. A smaller absolute bias is found at the rural OHP station. Compared to the current operational GDP 4.8 product, the GDP 4.9 dataset is a significant improvement. Although GOME-2 measurements are still underestimating the tropospheric NO<sub>2</sub> columns with respect to the ground data, the absolute and relative differences with the different MAXDOAS stations are smaller, both for the original comparisons and for the comparisons with the smoothed MAXDOAS columns.

In the future, the AMF calculation will be further improved, since uncertainty in AMF is one dominating source of errors in the tropospheric NO<sub>2</sub> retrieval, especially over polluted areas. The surface bidirectional reflectance distribution function (BRDF) effect will be included using a direction-dependent LER climatology from GOME-2 (L. Gijbert Tilstra, personal communication, 2018) to describe the angular distribution of the surface reflectance. Aerosol properties will be considered explicitly in the RTM calculation using ground-based aerosol observations from, e.g. MAXDOAS instruments, Mie scattering lidars, or sun photometers operated by the AEROSOL ROBOTIC NETWORK (AERONET). A priori NO<sub>2</sub> profiles from different global and regional models will help to analyse the effect of spatial resolution, temporal resolution, and emissions on the tropospheric NO<sub>2</sub> retrieval for GOME-2. Furthermore, the NO<sub>2</sub> algorithm will be adapted to measurements from the TROPOMI instrument with a spatial resolution as high as  $7\text{ km} \times 3.5\text{ km}$ .

*Data availability.* The current operational (GDP 4.8) NO<sub>2</sub> data from GOME-2 can be ordered via the FTP server and the EUMETSAT Data Centre (<https://acsaf.org/>, last access: 1 February 2019). The improved (GDP 4.9) dataset is currently available upon request.

*Supplement.* The supplement related to this article is available online at: <https://doi.org/10.5194/amt-12-1029-2019-supplement>.

*Competing interests.* The authors declare that they have no conflict of interest.

*Acknowledgements.* This work is funded by the DLR-DAAD Research Fellowships 2015 (57186656) programme with reference number 91585186 and is undertaken in the framework of the EUMETSAT AC-SAF project. We acknowledge the Belgian Science Policy Office (BELSPO) supporting part of this work through the PRODEX project B-ACSAF. We thank EUMETSAT for the ground segment interfacing work and for the provision of GOME-2 level 1 products. We thank the UPAS team for the development work on the UPAS system at DLR. We are thankful to Rüdiger Lang (EUMETSAT) for providing the GOME-2 level 1b testing data, Vincent Huijnen (KNMI) for providing the C-IFS model data, Gijsbert Tilstra (KNMI) for discussions on surface albedo, and Henk Eskes (KNMI) for creating the TM5-MP a priori NO<sub>2</sub> profiles. We acknowledge the free use of GOME-2 NO<sub>2</sub> column data from the QA4ECV project available at <http://www.qa4ecv.eu>. We also acknowledge the free use of the GOME-2 surface LER database created by KNMI and provided through the AC-SAF of EUMETSAT.

The article processing charges for this open-access publication were covered by a Research Centre of the Helmholtz Association.

Edited by: Jun Wang

Reviewed by: Kai Yang and one anonymous referee

## References

- Azam, F., Richter, A., Weber, M., Noë, S., and Burrows, J.: GOME-2 on MetOp-B Follow-on analysis of GOME2 in orbit degradation, Tech. rep., EUM/CO/09/460000696/RM, Final Report, IUP University of Bremen, 2015.
- Barkley, M. P., Smedt, I. D., Van Roozendaal, M., Kurosu, T. P., Chance, K., Arneth, A., Hagberg, D., Guenther, A., Paulot, F., Marais, E., and Mao, J.: Top-down isoprene emissions over tropical South America inferred from SCIAMACHY and OMI formaldehyde columns, *J. Geophys. Res.-Atmos.*, 118, 6849–6868, 2013.
- Beirle, S., Hörmann, C., Jöckel, P., Liu, S., Penning de Vries, M., Pozzer, A., Sihler, H., Valks, P., and Wagner, T.: The STRatospheric Estimation Algorithm from Mainz (STREAM): estimating stratospheric NO<sub>2</sub> from nadir-viewing satellites by weighted convolution, *Atmos. Meas. Tech.*, 9, 2753–2779, <https://doi.org/10.5194/amt-9-2753-2016>, 2016.
- Beirle, S., Lampel, J., Lerot, C., Sihler, H., and Wagner, T.: Parameterizing the instrumental spectral response function and its changes by a super-Gaussian and its derivatives, *Atmos. Meas. Tech.*, 10, 581–598, <https://doi.org/10.5194/amt-10-581-2017>, 2017.
- Boersma, K., Bucsele, E., Brinksma, E., and Gleason, J.: OMI algorithm theoretical basis document: OMI trace gas algorithms, vol. 4, edited by: Chance, K., Rep. ATBD-OMI, p. 19, 2002.
- Boersma, K., Eskes, H., and Brinksma, E.: Error analysis for tropospheric NO<sub>2</sub> retrieval from space, *J. Geophys. Res.-Atmos.*, 109, <https://doi.org/10.1029/2003JD003962>, 2004.
- Boersma, K. F., Eskes, H. J., Richter, A., De Smedt, I., Lorente, A., Beirle, S., van Geffen, J. H. G. M., Zara, M., Peters, E., Van Roozendaal, M., Wagner, T., Maasackers, J. D., van der A, R. J., Nightingale, J., De Rudder, A., Irie, H., Pinardi, G., Lambert, J.-C., and Compernelle, S. C.: Improving algorithms and uncertainty estimates for satellite NO<sub>2</sub> retrievals: results from the quality assurance for the essential climate variables (QA4ECV) project, *Atmos. Meas. Tech.*, 11, 6651–6678, [doi:10.5194/amt-11-6651-2018](https://doi.org/10.5194/amt-11-6651-2018), 2018.
- Boersma, K. F., Eskes, H. J., Dirksen, R. J., van der A, R. J., Veefkind, J. P., Stammes, P., Huijnen, V., Kleipool, Q. L., Sneep, M., Claas, J., Leitão, J., Richter, A., Zhou, Y., and Brunner, D.: An improved tropospheric NO<sub>2</sub> column retrieval algorithm for the Ozone Monitoring Instrument, *Atmos. Meas. Tech.*, 4, 1905–1928, <https://doi.org/10.5194/amt-4-1905-2011>, 2011.
- Boersma, K. F., Vinken, G. C. M., and Eskes, H. J.: Representativeness errors in comparing chemistry transport and chemistry climate models with satellite UV-Vis tropospheric column retrievals, *Geosci. Model Dev.*, 9, 875–898, <https://doi.org/10.5194/gmd-9-875-2016>, 2016.
- Bovensmann, H., Burrows, J., Buchwitz, M., Frerick, J., Rozanov, V., Chance, K., and Goede, A.: SCIAMACHY: Mission objectives and measurement modes, *J. Atmos. Sci.*, 56, 127–150, 1999.
- Brion, J., Chakir, A., Charbonnier, J., Daumont, D., Parisse, C., and Malicet, J.: Absorption spectra measurements for the ozone molecule in the 350–830 nm region, *J. Atmos. Chem.*, 30, 291–299, 1998.
- Bucsele, E. J., Krotkov, N. A., Celarier, E. A., Lamsal, L. N., Swartz, W. H., Bhartia, P. K., Boersma, K. F., Veefkind, J. P., Gleason, J. F., and Pickering, K. E.: A new stratospheric and tropospheric NO<sub>2</sub> retrieval algorithm for nadir-viewing satellite instruments: applications to OMI, *Atmos. Meas. Tech.*, 6, 2607–2626, <https://doi.org/10.5194/amt-6-2607-2013>, 2013.
- Burrows, J. P., Weber, M., Buchwitz, M., Rozanov, V., Ladstätter-Weißmayer, A., Richter, A., DeBeek, R., Hoogen, R., Bramstedt, K., Eichmann, K.-U., Eisinger, M., and Perner, D.: The global ozone monitoring experiment (GOME): Mission concept and first scientific results, *J. Atmos. Sci.*, 56, 151–175, 1999.
- Callies, J., Corpaccioli, E., Eisinger, M., Hahne, A., and Lefebvre, A.: GOME-2-Metop's second-generation sensor for operational ozone monitoring, *ESA bulletin*, 102, 28–36, 2000.
- Castellanos, P., Boersma, K. F., Torres, O., and de Haan, J. F.: OMI tropospheric NO<sub>2</sub> air mass factors over South America: effects of biomass burning aerosols, *Atmos. Meas. Tech.*, 8, 3831–3849, <https://doi.org/10.5194/amt-8-3831-2015>, 2015.
- Celarier, E. A., Brinksma, E. J., Gleason, J. F., Veefkind, J. P., Cede, A., Herman, J. R., Ionov, D., Goutail, F., Pommereau, J.-P., Lambert, J.-C., van Roozendaal, M., Pinardi, G., Wittrock, F., Schönhardt, A., Richter, A., Ibrahim, O. W., Wagner, T., Bojkov, B., Mount, G., Spinei, E., Chen, C. M., Pongetti, T. J., Sander, S. P., Bucsele, E. J., Wenig, M. O., Swart, D. P. J., Volten, H., Kroon, M., and Levelt, P. F.: Validation of Ozone Monitoring Instru-

- ment nitrogen dioxide columns, *J. Geophys. Res. Atmos.*, 113, <https://doi.org/10.1029/2007JD008908>, 2008.
- Chance, K. and Kurucz, R.: An improved high-resolution solar reference spectrum for earth's atmosphere measurements in the ultraviolet, visible, and near infrared, *J. Quant. Spectrosc. Ra.*, 111, 1289–1295, 2010.
- Chen, D., Zhou, B., Beirle, S., Chen, L. M., and Wagner, T.: Tropospheric NO<sub>2</sub> column densities deduced from zenith-sky DOAS measurements in Shanghai, China, and their application to satellite validation, *Atmos. Chem. Phys.*, 9, 3641–3662, <https://doi.org/10.5194/acp-9-3641-2009>, 2009.
- Chimot, J., Veeffkind, J. P., de Haan, J. F., Stammes, P., and Levelt, P. F.: Minimizing aerosol effects on the OMI tropospheric NO<sub>2</sub> retrieval – An improved use of the 477 nm O<sub>2</sub>–O<sub>2</sub> band and an estimation of the aerosol correction uncertainty, *Atmos. Meas. Tech. Discuss.*, <https://doi.org/10.5194/amt-2018-247>, in review, 2018.
- Clémer, K., Van Roozendael, M., Fayt, C., Hendrick, F., Hermans, C., Pinardi, G., Spurr, R., Wang, P., and De Mazière, M.: Multiple wavelength retrieval of tropospheric aerosol optical properties from MAXDOAS measurements in Beijing, *Atmos. Meas. Tech.*, 3, 863–878, <https://doi.org/10.5194/amt-3-863-2010>, 2010.
- Danckaert, T., Fayt, C., Van Roozendael, M., De Smedt, I., Letocart, V., Merlaud, A., and Pinardi, G.: QDOAS software user manual 2.109, IASB/BIRA, Uccle, Belgium, available at: <http://uvvis.aeronomie.be/software/QDOAS> (last access: 19 September 2015), 2015.
- De Smedt, I., Van Roozendael, M., Stavrou, T., Müller, J.-F., Lerot, C., Theys, N., Valks, P., Hao, N., and van der A, R.: Improved retrieval of global tropospheric formaldehyde columns from GOME-2/MetOp-A addressing noise reduction and instrumental degradation issues, *Atmos. Meas. Tech.*, 5, 2933–2949, <https://doi.org/10.5194/amt-5-2933-2012>, 2012.
- Dikty, S., Richter, A., Weber, M., Noël, S., Bovensmann, H., Wittrock, F., and Burrows, J.: GOME-2 on MetOp-A Support for Analysis of GOME-2 In-Orbit Degradation and Impacts on Level 2 Data Products—Final Report, Tech. rep., ITT 09/10000262, IUP University of Bremen, 2011.
- Ding, J., Miyazaki, K., van der A, R. J., Mijling, B., Kurokawa, J.-I., Cho, S., Janssens-Maenhout, G., Zhang, Q., Liu, F., and Levelt, P. F.: Intercomparison of NO<sub>x</sub> emission inventories over East Asia, *Atmos. Chem. Phys.*, 17, 10125–10141, <https://doi.org/10.5194/acp-17-10125-2017>, 2017.
- Doicu, A., Trautmann, T., and Schreier, F.: Numerical regularization for atmospheric inverse problems, Springer Science & Business Media, 2010.
- Drosoglou, T., Bais, A. F., Zyrichidou, I., Kouremeti, N., Poupkou, A., Liora, N., Giannaros, C., Koukouli, M. E., Balis, D., and Melas, D.: Comparisons of ground-based tropospheric NO<sub>2</sub> MAX-DOAS measurements to satellite observations with the aid of an air quality model over the Thessaloniki area, Greece, *Atmos. Chem. Phys.*, 17, 5829–5849, <https://doi.org/10.5194/acp-17-5829-2017>, 2017.
- Drosoglou, T., Koukouli, M. E., Kouremeti, N., Bais, A. F., Zyrichidou, I., Balis, D., van der A, R. J., Xu, J., and Li, A.: MAX-DOAS NO<sub>2</sub> observations over Guangzhou, China; ground-based and satellite comparisons, *Atmos. Meas. Tech.*, 11, 2239–2255, <https://doi.org/10.5194/amt-11-2239-2018>, 2018.
- Eskes, H. J. and Boersma, K. F.: Averaging kernels for DOAS total-column satellite retrievals, *Atmos. Chem. Phys.*, 3, 1285–1291, <https://doi.org/10.5194/acp-3-1285-2003>, 2003.
- EUMETSAT: GOME-2 Products Guide, Tech. rep., Ref.: EUM/OPSEPS/MAN/07/0445, Issue: v2D, 2009.
- EUMETSAT: GOME-2/Metop-A Level 1B Product Validation Report No. 5: Status at Reprocessing, Tech. rep., EUM/OPS/EPS/REP/09/0619, v1F, 2012.
- EUMETSAT: GOME-2 Newsletter Archive, Tech. rep., EUM/OPS-EPS/TEN/09/0552, 2015.
- European Commission: The EU Environmental Implementation Review: Common challenges and how to combine efforts to deliver better results, Tech. rep., Ref.: SWD(2017)33-60 fina, 2017.
- Gielen, C., Hendrick, F., Pinardi, G., De Smedt, I., Fayt, C., Hermans, C., Stavrou, T., Bauwens, M., Müller, J.-F., Ndenzako, E., Nzohabonayo, P., Akimana, R., Niyonzima, S., Van Roozendael, M., and De Mazière, M.: Characterisation of Central-African aerosol and trace-gas emissions based on MAX-DOAS measurements and model simulations over Bujumbura, Burundi, *Atmos. Chem. Phys. Discuss.*, <https://doi.org/10.5194/acp-2016-1104>, in review, 2017.
- Granier, C., Bessagnet, B., Bond, T., D'Angiola, A., van Der Gon, H. D., Frost, G. J., Heil, A., Kaiser, J. W., Kinne, S., Klimont, Z., Kloster, S., Lamarque, J.-F., Liousse, C., Masui, T., Meleux, F., Mieville, A., Ohara, T., Raut, J.-C., Riahi, K., Schultz, M. G., Smith, S. J., Thompson, A., van Aardenne, J., van der Werf, G. R., and van Vuuren, D. P.: Evolution of anthropogenic and biomass burning emissions of air pollutants at global and regional scales during the 1980–2010 period, *Clim. Change*, 109, p. 163, 2011.
- Gu, D., Wang, Y., Smeltzer, C., and Boersma, K. F.: Anthropogenic emissions of NO<sub>x</sub> over China: Reconciling the difference of inverse modeling results using GOME-2 and OMI measurements, *J. Geophys. Res.-Atmos.*, 119, 7732–7740, 2014.
- Hassinen, S., Balis, D., Bauer, H., Begoin, M., Delcloo, A., Eleftheratos, K., Gimeno Garcia, S., Granville, J., Grossi, M., Hao, N., Hedelt, P., Hendrick, F., Hess, M., Heue, K.-P., Hovila, J., Jönch-Sørensen, H., Kalakoski, N., Kauppi, A., Kiemle, S., Kins, L., Koukouli, M. E., Kujanpää, J., Lambert, J.-C., Lang, R., Lerot, C., Loyola, D., Pedernana, M., Pinardi, G., Romahn, F., van Roozendael, M., Lutz, R., De Smedt, I., Stammes, P., Steinbrecht, W., Tamminen, J., Theys, N., Tilstra, L. G., Tuinder, O. N. E., Valks, P., Zerefos, C., Zimmer, W., and Zyrichidou, I.: Overview of the O3M SAF GOME-2 operational atmospheric composition and UV radiation data products and data availability, *Atmos. Meas. Tech.*, 9, 383–407, <https://doi.org/10.5194/amt-9-383-2016>, 2016.
- Heckel, A., Richter, A., Tarsu, T., Wittrock, F., Hak, C., Pundt, I., Junkermann, W., and Burrows, J. P.: MAX-DOAS measurements of formaldehyde in the Po-Valley, *Atmos. Chem. Phys.*, 5, 909–918, <https://doi.org/10.5194/acp-5-909-2005>, 2005.
- Heckel, A., Kim, S.-W., Frost, G. J., Richter, A., Trainer, M., and Burrows, J. P.: Influence of low spatial resolution a priori data on tropospheric NO<sub>2</sub> satellite retrievals, *Atmos. Meas. Tech.*, 4, 1805–1820, <https://doi.org/10.5194/amt-4-1805-2011>, 2011.
- Hendrick, F., Müller, J.-F., Clémer, K., Wang, P., De Mazière, M., Fayt, C., Gielen, C., Hermans, C., Ma, J. Z., Pinardi, G., Stavrou, T., Vlemmix, T., and Van Roozendael, M.: Four years of ground-based MAX-DOAS observations of HONO and

- NO<sub>2</sub> in the Beijing area, *Atmos. Chem. Phys.*, 14, 765–781, <https://doi.org/10.5194/acp-14-765-2014>, 2014.
- Hilboll, A., Richter, A., and Burrows, J. P.: Long-term changes of tropospheric NO<sub>2</sub> over megacities derived from multiple satellite instruments, *Atmos. Chem. Phys.*, 13, 4145–4169, <https://doi.org/10.5194/acp-13-4145-2013>, 2013.
- Hilboll, A., Richter, A., and Burrows, J. P.: NO<sub>2</sub> pollution over India observed from space – the impact of rapid economic growth, and a recent decline, *Atmos. Chem. Phys. Discuss.*, <https://doi.org/10.5194/acp-2017-101>, in review, 2017.
- Holben, B., Eck, T., and Fraser, R.: Temporal and spatial variability of aerosol optical depth in the Sahel region in relation to vegetation remote sensing, *Int. J. Remote Sens.*, 12, 1147–1163, 1991.
- Hönninger, G., von Friedeburg, C., and Platt, U.: Multi axis differential optical absorption spectroscopy (MAX-DOAS), *Atmos. Chem. Phys.*, 4, 231–254, <https://doi.org/10.5194/acp-4-231-2004>, 2004.
- Horowitz, L. W., Walters, S., Mauzerall, D. L., Emmons, L. K., Rasch, P. J., Granier, C., Tie, X., Lamarque, J.-F., Schultz, M. G., Tyndall, G. S., Orlando, J. J., and Brasseur, G. P.: A global simulation of tropospheric ozone and related tracers: Description and evaluation of MOZART, version 2, *J. Geophys. Res. Atmos.*, 108, <https://doi.org/10.1029/2002JD002853>, 2003.
- Huijnen, V., Williams, J., van Weele, M., van Noije, T., Krol, M., Dentener, F., Segers, A., Houweling, S., Peters, W., de Laat, J., Boersma, F., Bergamaschi, P., van Velthoven, P., Le Sager, P., Eskes, H., Alkemade, F., Scheele, R., Nédélec, P., and Pätz, H.-W.: The global chemistry transport model TM5: description and evaluation of the tropospheric chemistry version 3.0, *Geosci. Model Dev.*, 3, 445–473, <https://doi.org/10.5194/gmd-3-445-2010>, 2010.
- Huijnen, V., Flemming, J., Chabrillat, S., Errera, Q., Christophe, Y., Blechschmidt, A.-M., Richter, A., and Eskes, H.: C-IFS-CB05-BASCOE: stratospheric chemistry in the Integrated Forecasting System of ECMWF, *Geosci. Model Dev.*, 9, 3071–3091, <https://doi.org/10.5194/gmd-9-3071-2016>, 2016.
- Ingmann, P., Veihelmann, B., Langen, J., Lamarre, D., Stark, H., and Courrèges-Lacoste, G. B.: Requirements for the GMES Atmosphere Service and ESA's implementation concept: Sentinel-4/5 and-5p, *Remote Sens. Environ.*, 120, 58–69, 2012.
- Irie, H., Takashima, H., Kanaya, Y., Boersma, K. F., Gast, L., Wittrock, F., Brunner, D., Zhou, Y., and Van Roozendael, M.: Eight-component retrievals from ground-based MAX-DOAS observations, *Atmos. Meas. Tech.*, 4, 1027–1044, <https://doi.org/10.5194/amt-4-1027-2011>, 2011.
- Irie, H., Boersma, K. F., Kanaya, Y., Takashima, H., Pan, X., and Wang, Z. F.: Quantitative bias estimates for tropospheric NO<sub>2</sub> columns retrieved from SCIAMACHY, OMI, and GOME-2 using a common standard for East Asia, *Atmos. Meas. Tech.*, 5, 2403–2411, <https://doi.org/10.5194/amt-5-2403-2012>, 2012.
- Kanaya, Y., Irie, H., Takashima, H., Iwabuchi, H., Akimoto, H., Sudo, K., Gu, M., Chong, J., Kim, Y. J., Lee, H., Li, A., Si, F., Xu, J., Xie, P.-H., Liu, W.-Q., Dzhola, A., Postlyakov, O., Ivanov, V., Grechko, E., Terpugova, S., and Panchenko, M.: Long-term MAX-DOAS network observations of NO<sub>2</sub> in Russia and Asia (MADRAS) during the period 2007–2012: instrumentation, elucidation of climatology, and comparisons with OMI satellite observations and global model simulations, *Atmos. Chem. Phys.*, 14, 7909–7927, <https://doi.org/10.5194/acp-14-7909-2014>, 2014.
- Kleipool, Q., Dobber, M., de Haan, J., and Levelt, P.: Earth surface reflectance climatology from 3 years of OMI data, *J. Geophys. Res.-Atmos.*, 113, <https://doi.org/10.1029/2008JD010290>, 2008.
- Kramer, L. J., Leigh, R. J., Remedios, J. J., and Monks, P. S.: Comparison of OMI and ground-based in situ and MAX-DOAS measurements of tropospheric nitrogen dioxide in an urban area, *J. Geophys. Res.-Atmos.*, 113, <https://doi.org/10.1029/2007JD009168>, 2008.
- Krotkov, N. A., Lamsal, L. N., Celarier, E. A., Swartz, W. H., Marchenko, S. V., Bucsela, E. J., Chan, K. L., Wenig, M., and Zara, M.: The version 3 OMI NO<sub>2</sub> standard product, *Atmos. Meas. Tech.*, 10, 3133–3149, <https://doi.org/10.5194/amt-10-3133-2017>, 2017.
- Kuhlmann, G., Lam, Y. F., Cheung, H. M., Hartl, A., Fung, J. C. H., Chan, P. W., and Wenig, M. O.: Development of a custom OMI NO<sub>2</sub> data product for evaluating biases in a regional chemistry transport model, *Atmos. Chem. Phys.*, 15, 5627–5644, <https://doi.org/10.5194/acp-15-5627-2015>, 2015.
- Lambert, J., Granville, J., Van Roozendael, M., Sarkissian, A., Goutail, F., Müller, J., Pommereau, J., and Russell III, J.: A climatology of NO<sub>2</sub> profile for improved air mass factors for ground-based vertical column measurements, in: *Proceedings of the 5th European Symposium Strat. Ozone*, Saint Jean de Luz, p. 703, 1999.
- Lampel, J., Pöhler, D., Tschirner, J., Frieß, U., and Platt, U.: On the relative absorption strengths of water vapour in the blue wavelength range, *Atmos. Meas. Tech.*, 8, 4329–4346, <https://doi.org/10.5194/amt-8-4329-2015>, 2015.
- Laughner, J. L., Zare, A., and Cohen, R. C.: Effects of daily meteorology on the interpretation of space-based remote sensing of NO<sub>2</sub>, *Atmos. Chem. Phys.*, 16, 15247–15264, <https://doi.org/10.5194/acp-16-15247-2016>, 2016.
- Laughner, J. L., Zhu, Q., and Cohen, R. C.: The Berkeley High Resolution Tropospheric NO<sub>2</sub> product, *Earth Syst. Sci. Data*, 10, 2069–2095, <https://doi.org/10.5194/essd-10-2069-2018>, 2018.
- Leitão, J., Richter, A., Vrekoussis, M., Kokhanovsky, A., Zhang, Q. J., Beekmann, M., and Burrows, J. P.: On the improvement of NO<sub>2</sub> satellite retrievals – aerosol impact on the airmass factors, *Atmos. Meas. Tech.*, 3, 475–493, <https://doi.org/10.5194/amt-3-475-2010>, 2010.
- Levelt, P., Van den Oord, G., Dobber, M., Malkki, A., Visser, H., de Vries, J., Stammes, P., Lundell, J., and Saari, H.: The Ozone Monitoring Instrument, *IEEE T. Geosci. Remote Sens.*, 44, 1093–1101, 2006.
- Lin, J.-T., Martin, R. V., Boersma, K. F., Sneep, M., Stammes, P., Spurr, R., Wang, P., Van Roozendael, M., Clémer, K., and Irie, H.: Retrieving tropospheric nitrogen dioxide from the Ozone Monitoring Instrument: effects of aerosols, surface reflectance anisotropy, and vertical profile of nitrogen dioxide, *Atmos. Chem. Phys.*, 14, 1441–1461, <https://doi.org/10.5194/acp-14-1441-2014>, 2014.
- Lin, J.-T., Liu, M.-Y., Xin, J.-Y., Boersma, K. F., Spurr, R., Martin, R., and Zhang, Q.: Influence of aerosols and surface reflectance on satellite NO<sub>2</sub> retrieval: seasonal and spatial characteristics and implications for NO<sub>x</sub> emission constraints, *Atmos. Chem. Phys.*, 15, 11217–11241, <https://doi.org/10.5194/acp-15-11217-2015>, 2015.

- Liu, F., Beirle, S., Zhang, Q., van der A, R. J., Zheng, B., Tong, D., and He, K.: NO<sub>x</sub> emission trends over Chinese cities estimated from OMI observations during 2005 to 2015, *Atmos. Chem. Phys.*, 17, 9261–9275, <https://doi.org/10.5194/acp-17-9261-2017>, 2017.
- Lorente, A., Folkert Boersma, K., Yu, H., Dörner, S., Hilboll, A., Richter, A., Liu, M., Lamsal, L. N., Barkley, M., De Smedt, I., Van Roozendael, M., Wang, Y., Wagner, T., Beirle, S., Lin, J.-T., Krotkov, N., Stammes, P., Wang, P., Eskes, H. J., and Krol, M.: Structural uncertainty in air mass factor calculation for NO<sub>2</sub> and HCHO satellite retrievals, *Atmos. Meas. Tech.*, 10, 759–782, <https://doi.org/10.5194/amt-10-759-2017>, 2017.
- Loyola, D., Thomas, W., Livschitz, Y., Ruppert, T., Albert, P., and Hollmann, R.: Cloud properties derived from GOME/ERS-2 backscatter data for trace gas retrieval, *IEEE T. Geosci. Remote Sens.*, 45, 2747–2758, 2007.
- Loyola, D., Koukouli, M., Valks, P., Balis, D., Hao, N., Van Roozendael, M., Spurr, R., Zimmer, W., Kiemle, S., Lerot, C., et al.: The GOME-2 total column ozone product: Retrieval algorithm and ground-based validation, *J. Geophys. Res.-Atmos.*, 116, <https://doi.org/10.1029/2010JD014675>, 2011.
- Loyola, D. G., Pedernana, M., and García, S. G.: Smart sampling and incremental function learning for very large high dimensional data, *Neural Networks*, 78, 75–87, 2016.
- Loyola, D. G., Gimeno García, S., Lutz, R., Argyrouli, A., Romahn, F., Spurr, R. J. D., Pedernana, M., Doicu, A., Molina García, V., and Schüssler, O.: The operational cloud retrieval algorithms from TROPOMI on board Sentinel-5 Precursor, *Atmos. Meas. Tech.*, 11, 409–427, <https://doi.org/10.5194/amt-11-409-2018>, 2018.
- Lutz, R., Loyola, D., Gimeno García, S., and Romahn, F.: OCRA radiometric cloud fractions for GOME-2 on MetOp-A/B, *Atmos. Meas. Tech.*, 9, 2357–2379, <https://doi.org/10.5194/amt-9-2357-2016>, 2016.
- Ma, J. Z., Beirle, S., Jin, J. L., Shaiganfar, R., Yan, P., and Wagner, T.: Tropospheric NO<sub>2</sub> vertical column densities over Beijing: results of the first three years of ground-based MAX-DOAS measurements (2008–2011) and satellite validation, *Atmos. Chem. Phys.*, 13, 1547–1567, <https://doi.org/10.5194/acp-13-1547-2013>, 2013.
- McLinden, C. A., Fioletov, V., Boersma, K. F., Kharol, S. K., Krotkov, N., Lamsal, L., Makar, P. A., Martin, R. V., Veefkind, J. P., and Yang, K.: Improved satellite retrievals of NO<sub>2</sub> and SO<sub>2</sub> over the Canadian oil sands and comparisons with surface measurements, *Atmos. Chem. Phys.*, 14, 3637–3656, <https://doi.org/10.5194/acp-14-3637-2014>, 2014.
- Miyazaki, K., Eskes, H., Sudo, K., Boersma, K. F., Bowman, K., and Kanaya, Y.: Decadal changes in global surface NO<sub>x</sub> emissions from multi-constituent satellite data assimilation, *Atmos. Chem. Phys.*, 17, 807–837, <https://doi.org/10.5194/acp-17-807-2017>, 2017.
- Müller, J.-P., Kharbouche, S., Gobron, N., Scanlon, T., Govaerts, Y., Danne, O., Schultz, J., Lattanzio, A., Peters, E., De Smedt, I., Beirle, S., Lorente, A., Coheur, P., George, M., Wagner, T., Hilboll, A., Richter, A., Van Roozendael, M., and Boersma, K.: Recommendations (scientific) on best practices for retrievals for Land and Atmosphere ECVs, *Tech. rep., Deliverable 4.2 – version 1.0*, 2016.
- Munro, R., Lang, R., Klaes, D., Poli, G., Retscher, C., Lindstrot, R., Huckle, R., Lacan, A., Grzegorski, M., Holdak, A., Kokhanovsky, A., Livschitz, J., and Eisinger, M.: The GOME-2 instrument on the Metop series of satellites: instrument design, calibration, and level 1 data processing – an overview, *Atmos. Meas. Tech.*, 9, 1279–1301, <https://doi.org/10.5194/amt-9-1279-2016>, 2016.
- Nolin, A., Armstrong, R., and Maslanik, J.: Near real-time SSM/I EASE-grid daily global ice concentration and snow extent, *Digital Media, National Snow and Ice Data Center, Boulder, CO, USA*, 2005.
- Nüß, H., Richter, A., Valks, P., and Burrows, J.: Improvement of the NO<sub>2</sub> total column retrieval for GOME-2, O3M SAF Visiting Scientist Activity, Final Report, IUP University of Bremen, 2006.
- Olivier, J. G., Bouwman, A., Berdowski, J., Veldt, C., Bloos, J., Visschedijk, A., Zandveld, P., and Haverlag, J.: Description of EDGAR Version 2.0: A set of global emission inventories of greenhouse gases and ozone-depleting substances for all anthropogenic and most natural sources on a per country basis and on 1 degree × 1 degree grid, RIVM report no. 771060 002/TNO-MEP report no. R96/119, <https://www.rivm.nl/bibliotheek/rapporten/771060002.pdf> (last access: 1 February 2019), 1996.
- Ortega, I., Koenig, T., Sinreich, R., Thomson, D., and Volkamer, R.: The CU 2-D-MAX-DOAS instrument – Part 1: Retrieval of 3-D distributions of NO<sub>2</sub> and azimuth-dependent OVOC ratios, *Atmos. Meas. Tech.*, 8, 2371–2395, <https://doi.org/10.5194/amt-8-2371-2015>, 2015.
- Penning de Vries, M. J. M., Beirle, S., Hörmann, C., Kaiser, J. W., Stammes, P., Tilstra, L. G., Tuinder, O. N. E., and Wagner, T.: A global aerosol classification algorithm incorporating multiple satellite data sets of aerosol and trace gas abundances, *Atmos. Chem. Phys.*, 15, 10597–10618, <https://doi.org/10.5194/acp-15-10597-2015>, 2015.
- Peters, E., Wittrock, F., Richter, A., Alvarado, L. M. A., Rozanov, V. V., and Burrows, J. P.: Liquid water absorption and scattering effects in DOAS retrievals over oceans, *Atmos. Meas. Tech.*, 7, 4203–4221, <https://doi.org/10.5194/amt-7-4203-2014>, 2014.
- Pinardi, G., Van Roozendael, M., Lambert, J.-C., Granville, J., Hendrick, F., Tack, F., Yu, H., Cede, A., Kanaya, Y., Irie, I., Goutail, F., Pommereau, J.-P., Pazmino, A., Wittrock, F., Richter, A., Wagner, T., Gu, M., Remmers, J., Friess, U., Vlemmix, T., PETERS, A., Hao, N., Tiefengraber, M., Herman, J., Abuhassan, N., Bais, A., Kouremeti, N., Hovila, J., Holla, R., Chong, J., Postylyakov, O., and Ma, J.: GOME-2 total and tropospheric NO<sub>2</sub> validation based on zenith-sky, direct-sun and multi-axis DOAS network observations, in: *Proc. of the 2014 EUMETSAT Meteorological Satellite Conference, Geneva, Switzerland, 22–26 September 2014, EUMETSAT*, 2014.
- Pinardi, G., Lambert, J.-C., Granville, J., Yu, H., De Smedt, I., van Roozendael, M., and Valks, P.: O3M-SAF validation report, *Tech. rep., SAF/O3M/IASB/VR/NO<sub>2</sub>/TN-IASB-GOME2-O3MSAF-NO<sub>2</sub>-2015, 1/1*, 2015.
- Platt, U. and Stutz, J.: *Differential Optical Absorption Spectroscopy*, Springer, 2008.
- Pope, R. M. and Fry, E. S.: Absorption spectrum (380–700 nm) of pure water. II. Integrating cavity measurements, *Appl. Opt.*, 36, 8710–8723, 1997.
- Richter, A. and verification team: S5P/TROPOMI Science Verification Report, *Tech. rep., S5P-IUP-L2-ScVR-RP issue 2.1*, 2015.

- Richter, A., Burrows, J. P., Nüß, H., Granier, C., and Niemeier, U.: Increase in tropospheric nitrogen dioxide over China observed from space, *Nature*, 437, p. 129, 2005.
- Richter, A., Begoin, M., Hilboll, A., and Burrows, J. P.: An improved NO<sub>2</sub> retrieval for the GOME-2 satellite instrument, *Atmos. Meas. Tech.*, 4, 1147–1159, <https://doi.org/10.5194/amt-4-1147-2011>, 2011.
- Rothman, L., Gordon, I., Barber, R., Dothe, H., Gamache, R., Goldman, A., Perevalov, V., Tashkun, S., and Tennyson, J.: HITEMP, the high-temperature molecular spectroscopic database, *J. Quant. Spectrosc. Ra.*, 111, 2139–2150, 2010.
- Russell, A. R., Perring, A. E., Valin, L. C., Bucsele, E. J., Browne, E. C., Wooldridge, P. J., and Cohen, R. C.: A high spatial resolution retrieval of NO<sub>2</sub> column densities from OMI: method and evaluation, *Atmos. Chem. Phys.*, 11, 8543–8554, <https://doi.org/10.5194/acp-11-8543-2011>, 2011.
- Safieddine, S., Clerbaux, C., George, M., Hadji-Lazaro, J., Hurtmans, D., Coheur, P.-F., Wespes, C., Loyola, D., Valks, P., and Hao, N.: Tropospheric ozone and nitrogen dioxide measurements in urban and rural regions as seen by IASI and GOME-2, *J. Geophys. Res.-Atmos.*, 118, 10555–10566, <https://doi.org/10.1002/jgrd.50669>, 2013.
- Seinfeld, J. H., Pandis, S., and Noone, K.: *Atmospheric chemistry and physics: from air pollution to climate change*, Wiley, 1998.
- Solomon, S.: Stratospheric ozone depletion: A review of concepts and history, *Rev. Geophys.*, 37, 275–316, 1999.
- Spurr, R., Kurosu, T., and Chance, K.: A linearized discrete ordinate radiative transfer model for atmospheric remote-sensing retrieval, *J. Quant. Spectrosc. Ra.*, 68, 689–735, 2001.
- Spurr, R. J.: VLIDORT: A linearized pseudo-spherical vector discrete ordinate radiative transfer code for forward model and retrieval studies in multilayer multiple scattering media, *J. Quant. Spectrosc. Ra.*, 102, 316–342, 2006.
- Thalman, R. and Volkamer, R.: Temperature dependent absorption cross-sections of O<sub>2</sub>–O<sub>2</sub> collision pairs between 340 and 630 nm and at atmospherically relevant pressure, *Phys. Chem. Chem. Phys.*, 15, 15371–15381, 2013.
- Tikhonov, A. and Arsenin, V.: *Solutions of ill-posed problems*, V. H. Winston & Sons, Washington, 1977.
- Tilstra, L., Tuinder, O., and Stammes, P.: GOME-2 surface LER product – Algorithm Theoretical Basis Document, Tech. rep., KNMI Report O3MSAF/KNMI/ATBD/003, Issue 2.2, 2017a.
- Tilstra, L., Wang, P., and Stammes, P.: Surface reflectivity climatologies from UV to NIR determined from Earth observations by GOME-2 and SCIAMACHY, *J. Geophys. Res.-Atmos.*, 122, 4084–4111, 2017b.
- Valks, P., Pinardi, G., Richter, A., Lambert, J.-C., Hao, N., Loyola, D., Van Roozendaal, M., and Emmadi, S.: Operational total and tropospheric NO<sub>2</sub> column retrieval for GOME-2, *Atmos. Meas. Tech.*, 4, 1491–1514, <https://doi.org/10.5194/amt-4-1491-2011>, 2011.
- Valks, P., Loyola, D., Hao, N., Hedelt, P., Slijkhuis, S., Grossi, M., Begoin, M., Gimeno Garcia, S., and Lutz, R.: Algorithm Theoretical Basis Document for GOME-2 Total Column Products of Ozone, NO<sub>2</sub>, BrO, SO<sub>2</sub>, H<sub>2</sub>O, HCHO and Cloud Properties (GDP 4.8 for AC SAF OTO and NTO), Tech. rep., SAF/AC/DLR/ATBD/01, Iss./Rev.: 3/A/2, 2017.
- van Geffen, J. H. G. M., Boersma, K. F., Van Roozendaal, M., Hendrick, F., Mahieu, E., De Smedt, I., Sneep, M., and Veefkind, J. P.: Improved spectral fitting of nitrogen dioxide from OMI in the 405–465 nm window, *Atmos. Meas. Tech.*, 8, 1685–1699, <https://doi.org/10.5194/amt-8-1685-2015>, 2015.
- van Geffen, J., Boersma, K., Eskes, H., Maasackers, J., and Veefkind, J.: TROPOMI ATBD of the total and tropospheric NO<sub>2</sub> data products, Tech. rep., S5P-KNMI-L2-0005-RP issue 1.0.0. KNMI, De Bilt, the Netherlands, 2016.
- Vandaele, A. C., Hermans, C., Fally, S., Carleer, M., Colin, R., Merienne, M.-F., Jenouvrier, A., and Coquart, B.: High-resolution Fourier transform measurement of the NO<sub>2</sub> visible and near-infrared absorption cross sections: Temperature and pressure effects, *J. Geophys. Res.-Atmos.*, 107, <https://doi.org/10.1029/2001JD000971>, 2002.
- van der A, R. J., Mijling, B., Ding, J., Koukouli, M. E., Liu, F., Li, Q., Mao, H., and Theys, N.: Cleaning up the air: effectiveness of air quality policy for SO<sub>2</sub> and NO<sub>x</sub> emissions in China, *Atmos. Chem. Phys.*, 17, 1775–1789, <https://doi.org/10.5194/acp-17-1775-2017>, 2017.
- Vasilkov, A., Qin, W., Krotkov, N., Lamsal, L., Spurr, R., Haffner, D., Joiner, J., Yang, E.-S., and Marchenko, S.: Accounting for the effects of surface BRDF on satellite cloud and trace-gas retrievals: a new approach based on geometry-dependent Lambertian equivalent reflectivity applied to OMI algorithms, *Atmos. Meas. Tech.*, 10, 333–349, <https://doi.org/10.5194/amt-10-333-2017>, 2017.
- Veefkind, J., Aben, I., McMullan, K., Förster, H., De Vries, J., Oter, G., Claas, J., Eskes, H., De Haan, J., Kleipool, Q., van Weele, M., Hasekamp, O., Hoogeveen, R., Landgraf, J., Snel, R., Tol, P., Ingmann, P., Voors, R., Kruizinga, B., Vink, R., Visser, H., and Levelt, P.: TROPOMI on the ESA Sentinel-5 Precursor: A GMES mission for global observations of the atmospheric composition for climate, air quality and ozone layer applications, *Remote Sens. Environ.*, 120, 70–83, 2012.
- Veefkind, J. P., de Haan, J. F., Sneep, M., and Levelt, P. F.: Improvements to the OMI O<sub>2</sub>–O<sub>2</sub> operational cloud algorithm and comparisons with ground-based radar–lidar observations, *Atmos. Meas. Tech.*, 9, 6035–6049, <https://doi.org/10.5194/amt-9-6035-2016>, 2016.
- Vlemmix, T., Hendrick, F., Pinardi, G., De Smedt, I., Fayt, C., Hermans, C., PETERS, A., Wang, P., Levelt, P., and Van Roozendaal, M.: MAX-DOAS observations of aerosols, formaldehyde and nitrogen dioxide in the Beijing area: comparison of two profile retrieval approaches, *Atmos. Meas. Tech.*, 8, 941–963, <https://doi.org/10.5194/amt-8-941-2015>, 2015.
- Vountas, M., Richter, A., Wittrock, F., and Burrows, J. P.: Inelastic scattering in ocean water and its impact on trace gas retrievals from satellite data, *Atmos. Chem. Phys.*, 3, 1365–1375, <https://doi.org/10.5194/acp-3-1365-2003>, 2003.
- Vrekoussis, M., Wittrock, F., Richter, A., and Burrows, J. P.: GOME-2 observations of oxygenated VOCs: what can we learn from the ratio glyoxal to formaldehyde on a global scale?, *Atmos. Chem. Phys.*, 10, 10145–10160, <https://doi.org/10.5194/acp-10-10145-2010>, 2010.
- Wagner, T., Dix, B. V., Friedeburg, C. V., Frieß, U., Sanghavi, S., Sinreich, R., and Platt, U.: MAX-DOAS O<sub>4</sub> measurements: A new technique to derive information on atmospheric aerosols – Principles and information content, *J. Geophys. Res.-Atmos.*, 109, <https://doi.org/10.1029/2004JD004904>, 2004.

- Wagner, T., Beirle, S., Brauers, T., Deutschmann, T., Friß, U., Hak, C., Halla, J. D., Heue, K. P., Junkermann, W., Li, X., Platt, U., and Pundt-Gruber, I.: Inversion of tropospheric profiles of aerosol extinction and HCHO and NO<sub>2</sub> mixing ratios from MAX-DOAS observations in Milano during the summer of 2003 and comparison with independent data sets, *Atmos. Meas. Tech.*, 4, 2685–2715, <https://doi.org/10.5194/amt-4-2685-2011>, 2011.
- Wang, Y., Beirle, S., Lampel, J., Koukouli, M., De Smedt, I., Theys, N., Li, A., Wu, D., Xie, P., Liu, C., Van Roozendael, M., Stavrakou, T., Müller, J.-F., and Wagner, T.: Validation of OMI, GOME-2A and GOME-2B tropospheric NO<sub>2</sub>, SO<sub>2</sub> and HCHO products using MAX-DOAS observations from 2011 to 2014 in Wuxi, China: investigation of the effects of priori profiles and aerosols on the satellite products, *Atmos. Chem. Phys.*, 17, 5007–5033, <https://doi.org/10.5194/acp-17-5007-2017>, 2017.
- Williams, J. E., Boersma, K. F., Le Sager, P., and Verstraeten, W. W.: The high-resolution version of TM5-MP for optimized satellite retrievals: description and validation, *Geosci. Model Dev.*, 10, 721–750, <https://doi.org/10.5194/gmd-10-721-2017>, 2017.
- Wittrock, F., Oetjen, H., Richter, A., Fietkau, S., Medeke, T., Rozanov, A., and Burrows, J. P.: MAX-DOAS measurements of atmospheric trace gases in Ny-Ålesund – Radiative transfer studies and their application, *Atmos. Chem. Phys.*, 4, 955–966, <https://doi.org/10.5194/acp-4-955-2004>, 2004.
- Wu, F. C., Xie, P. H., Li, A., Chan, K. L., Hartl, A., Wang, Y., Si, F. Q., Zeng, Y., Qin, M., Xu, J., Liu, J. G., Liu, W. Q., and Wenig, M.: Observations of SO<sub>2</sub> and NO<sub>2</sub> by mobile DOAS in the Guangzhou eastern area during the Asian Games 2010, *Atmos. Meas. Tech.*, 6, 2277–2292, <https://doi.org/10.5194/amt-6-2277-2013>, 2013.
- Zara, M., Boersma, K. F., De Smedt, I., Richter, A., Peters, E., van Geffen, J. H. G. M., Beirle, S., Wagner, T., Van Roozendael, M., Marchenko, S., Lamsal, L. N., and Eskes, H. J.: Improved slant column density retrieval of nitrogen dioxide and formaldehyde for OMI and GOME-2A from QA4ECV: intercomparison, uncertainty characterisation, and trends, *Atmos. Meas. Tech.*, 11, 4033–4058, <https://doi.org/10.5194/amt-11-4033-2018>, 2018.
- Zien, A. W., Richter, A., Hilboll, A., Blechschmidt, A.-M., and Burrows, J. P.: Systematic analysis of tropospheric NO<sub>2</sub> long-range transport events detected in GOME-2 satellite data, *Atmos. Chem. Phys.*, 14, 7367–7396, <https://doi.org/10.5194/acp-14-7367-2014>, 2014.